ABSOLUTE DETECTION OF $O_2(a^1\Delta)$ CONCENTRATIONS

P. Keating
L. Hanko
C. A. Helms
G. P. Perram

DTIC
ELECTE
JUN 17 1992
S D
A

March 1992

Final Report

Weapons Laboratory
Air Force Systems Command
Kirtland Air Force Base, NM 87117-6008

92-15499

92 6 15 038

This report was prepared by the Phillips Laboratory, Kirtland Air Force Base, New Mexico, under Job Order 36470199. The Laboratory Project-Officer-in-Charge was Charles A. Helms (LIDB).

When Government drawings, specifications, or other data are used for any purpose other than in connection with a definitely Government-related procurement, the United States Government incurs no responsibility or any obligation whatsoever. The fact that the Government may have formulated or in any way supplied the said drawings, specifications, or other data, is not to be regarded by implication, or otherwise in any manner construed, as licensing the holder, or any other person or corporation; or as conveying any rights or permission to manufacture, use, or sell any patented invention that may in any way be related thereto.

This report has been authored by employees of the United States Government. Accordingly, the United States Government retains a nonexclusive, royalty-free license to publish or reproduce the material contained herein, or allow others to do so, for the United States Government purposes.

If your address has changed, if you wish to be removed from the mailing list, or if your organization no longer employs the addressee, please notify PL/LIDB Kirtland AFB, NM 87117-6008, to help maintain a current mailing list.

This report has been reviewed by the Public Affairs Office and is releasable to the National Technical Information Service (NTIS). At NTIS, it will be available to the general public, including foreign nationals.

This technical report has been reviewed and is approved for publication.

CHARLES A. HELMS
Project Officer

FOR THE COMMANDER

STEVEN E. LAMBERSON   ROBERT C. LIGDAY
Lieutenant Colonel, USAF   Lieutenant Colonel, USAF
Chief, Applied Laser   Chief, Laser Systems Division
   Technology Branch

DO NOT RETURN COPIES OF THIS REPORT UNLESS CONTRACTUAL OBLIGATIONS OR NOTICE ON A SPECIFIC DOCUMENT REQUIRES THAT IT BE RETURNED.

REPORT DOCUMENTATION PAGE

Public reporting burden for this collection of information is estimated to average 1 hour per response, including the time for reviewing instructions, searching existing data sources, gathering and maintaining the data needed, and completing and reviewing the collection of information. Send comments regarding this burden estimate or any other aspect of this collection of information, including suggestions for reducing this burden, to Washington Headquarters Services, Directorate for Information Operations and Reports, 1215 Jefferson Davis Highway, Suite 1204, Arlington, VA 22202-4302, and to the Office of Management and Budget, Paperwork Reduction Project (0704-0188), Washington, DC 20503.

1. AGENCY USE ONLY (Leave blank)	2. REPORT DATE March 1992	3. REPORT TYPE AND DATES COVERED Final Report; Sep 86 - Mar 90

4. TITLE AND SUBTITLE

ABSOLUTE DETECTION OF $O_2(a^1\Delta)$ CONCENTRATIONS

5. FUNDING NUMBERS

PE: 63605F
PR: 3647
TA: 01
WU: 99

6. AUTHOR(S)

Keating, P., Hanko, L., Helms, C. A., and
Perram, G. P.

7. PERFORMING ORGANIZATION NAME(S) AND ADDRESS(ES)

8. PERFORMING ORGANIZATION REPORT NUMBER

9. SPONSORING / MONITORING AGENCY NAME(S) AND ADDRESS(ES)

Phillips Laboratory
Kirtland AFB, NM 87117-6008

10. SPONSORING / MONITORING AGENCY REPORT NUMBER

WL-TR-90-85

11. SUPPLEMENTARY NOTES

12a. DISTRIBUTION / AVAILABILITY STATEMENT

Approved for public release; Distribution Unlimited.

12b. DISTRIBUTION CODE

13. ABSTRACT (Maximum 200 words)

The design and calibration of a system for measuring absolute concentrations of $O_2(a^1\Delta)$ produced in the Chemical Oxygen-Iodine Laser (COIL) are presented. The detection system features a liquid-nitrogen-cooled intrinsic germanium detector calibrated using gas-phase Electron Paramagnetic Resonance (EPR) Spectroscopy. Theoretical expressions relating the measured EPR signals to absolute $O_2(a^1\Delta)$ concentrations are reviewed, and error analysis is included.

14. SUBJECT TERMS Infrared Detection, Calibration Using EPR, Singlet
Delta Oxygen Yield, Calibration of Singlet Delta
Oxygen

15. NUMBER OF PAGES 89

16. PRICE CODE

17. SECURITY CLASSIFICATION OF REPORT	18. SECURITY CLASSIFICATION OF THIS PAGE	19. SECURITY CLASSIFICATION OF ABSTRACT	20. LIMITATION OF ABSTRACT
UNCLASSIFIED	UNCLASSIFIED	UNCLASSIFIED	SAR

PREFACE

The authors of this report would like to acknowledge the helpful review of previous calibration procedures and the insights provided by these participants in the COIL Diagnostics Technical Interchange meeting held at the Aerospace Corporation on 5 November 1986.

R. F. Heidner
Aerospace Corporation

D. N. Plummer
R&D Associates

I. B. Goldberg
Rockwell Science Center

J. O. Berg
TRW Space and Technology Group

K. A. Truesdell
Phillips Laboratory

A. M. Falick
Univ. of California at San Francisco

G. Schneider
Rocketdyne

A. Horowitz
TRW Space and Technology Group

The purpose of this report is to: (1) document the $O_2(a^1\Delta)$ diagnostics and calibration procedures used for the ROTOCOIL test program, (2) establish a baseline calibration apparatus and procedure for various COIL research groups, (3) review the status of absolute $O_2(a^1\Delta)$ detection methods, and (4) introduce spectroscopic and radiometric techniques to the novice researcher.

Accesion For	
NTIS CRA&I	☑
DTIC TAB	☐
Unannounced	☐
Justification	
By	
Distribution /	
Availability Codes	
Dist	Avail and / or Special
A-1	

CONTENTS

FIGURES

FIGURES (Continued)

TABLES

1.0 INTRODUCTION

The Chemical Oxygen-Iodine Laser (COIL) is the shortest wavelength high energy chemical laser in existence today and has great potential for Air Force directed energy weapons applications. The Phillips Laboratory (PL), Kirtland Air Force Base, New Mexico, is vigorously pursuing the development of efficient, scalable COIL devices with high output power and excellent beam quality. While chemical oxygen-iodine lasers are in the early stages of large scale development, a 25-kW device is being tested at the PL and scaling to larger devices is under active investigation.

The performance of COIL devices strongly depends on the absolute concentration and yield of the metastable energy carrier, singlet oxygen. The total energy density available in the COIL flow is determined by the concentration of $O_2(a^1\Delta)$; however, the extractable energy is limited by the yield, defined as the ratio $[O_2(^1\Delta)]/[O_2(X^3\Sigma)]$ (Ref. 1). Since typical chemical oxygen generators operate near the threshold yield, the laser power is sensitive to small changes in singlet oxygen concentrations (Ref. 2). Without reliable measurements of singlet oxygen, it is impossible to separate the effects of oxygen generator performance, iodine nozzle mixing efficiency, and cavity transport on attained laser power. The performance of chemical singlet-oxygen generators is best determined by the absolute measurement of singlet-oxygen concentrations. Additionally, the study of COIL gas phase kinetics often requires diagnostics for absolute $O_2(^1\Delta)$ concentrations (Ref. 3). Thus, the accurate, absolute measurement of $O_2(a^1\Delta)$ is critical to predicting, characterizing, and modeling the performance of COIL devices.

One method to measure $O_2(a^1\Delta)$ concentration is to observe its spontaneous emission with a detector calibrated using Electron Paramagnetic Resonance (EPR) spectroscopy (Ref. 4). Both ground state, $X^3\Sigma$, and excited state, $a^1\Delta$ oxygen have been studied using EPR. In fact, ground state oxygen is often used as a quantitative standard for EPR (Ref. 5). The EPR spectrum of $O_2(^1\Delta)$ was first reported in 1965 (Ref. 6), and has received considerable attention both theoretically and experimentally (Refs. 7-9). Indeed, EPR spectroscopy

1

is currently the most reliable technique for measuring the concentration of $O_2(^1\Delta)$ under low pressure, gas phase conditions (Ref. 4). By observing the relative EPR spectral areas of $O_2(X^3\Sigma)$ and $O_2(a^1\Delta)$ in a pure oxygen flow, a standard for the absolute concentrations of these species is established (Ref.4). If the infrared emission from the $O_2(a-X)$ transition is simultaneously observed, then a method for calibrating the emission detector is provided. This technique has been used extensively to characterize the performance of COIL devices (Refs. 4, 10-12).

Conceptually the method is straightforward but many experimental and analytical issues limit the accuracy. In this report, an attempt will be made to clearly define and reduce the most important systematic and statistical errors and to provide suggestions for designing a reliable experimental apparatus for the calibration and operation of such a diagnostic on COIL devices. Specifically, the following issues will be addressed: derivation of the theoretical expressions required for absolute $O_2(a^1\Delta)$ concentration measurements (Section 2.0), characterization of a reliable, accurate calibration apparatus (Section 3.0), analysis of observed spectra and emission signals (Section 4.0), and a detailed error analysis (Section 5.0).

2.0 BACKGROUND THEORY

Theoretical expressions relating measured EPR signals to absolute oxygen concentrations and observed infrared detector signals will be reviewed in this section. A background discussion of spectroscopy, kinetics, and radiometry is provided to assist in this development.

2.1 ELECTRONIC STRUCTURE OF OXYGEN

Oxygen atoms have ground state electronic configurations $1s^2 2s^2 2p^4$. The two unfilled 2p orbitals are equivalent to two electrons with $l = 1$, $s = 1/2$ yielding 15 distinct states (Ref. 13). Using a Slater Diagram, the three multiplets ^3P, ^1D, and ^1S are readily identified. The spin-orbit splitting of the ^3P term to form the $^3P_2$, $^3P_1$, and $^3P_0$ levels is small with the energies of these levels being 0, 158.5 and 221.5 cm^{-1}, respectively (Ref. 14) . The triplet term, ^3P, is the lowest in energy with the singlet ^1D and ^1S terms higher by 1.967 and 4.188 eV, respectively (Ref. 14).

The molecular orbitals for diatomic oxygen may be formed from linear combinations of the atomic orbitals (Refs. 10-16). Figure 1 illustrates the atomic orbitals and the resulting molecular orbitals for oxygen. The filling of these molecular orbitals by the 16 electrons of O_2 is denoted by the arrows indicating spin up ($m_s = +1/2$) or down ($m_s = -1/2$). The configuration of Figure 1 may be written

$$(1\sigma_g)^2(1\sigma_u)^2(2\sigma_g)^2(2\sigma_u)^2(3\sigma_g)^2(1\pi_u)^4(1\pi_g)^2(3\sigma_u)^0$$

where the superscripts denote the number of electrons in the given orbital. Typically this notation is shortened to 2420 for the occupancy of the last four orbitals. The antibonding orbital, $1\pi_g$, is only partially filled and there are six unique ways for the two electrons to occupy this orbital. The 6 arrangements resulting in 6 possible electronic levels are shown in Figure 2. The appropriate antisymmetric wavefunctions are described in Reference 17. The ground electronic state is $X^3\Sigma_g^-$ and the first two excited states are $a^1\Delta_g$
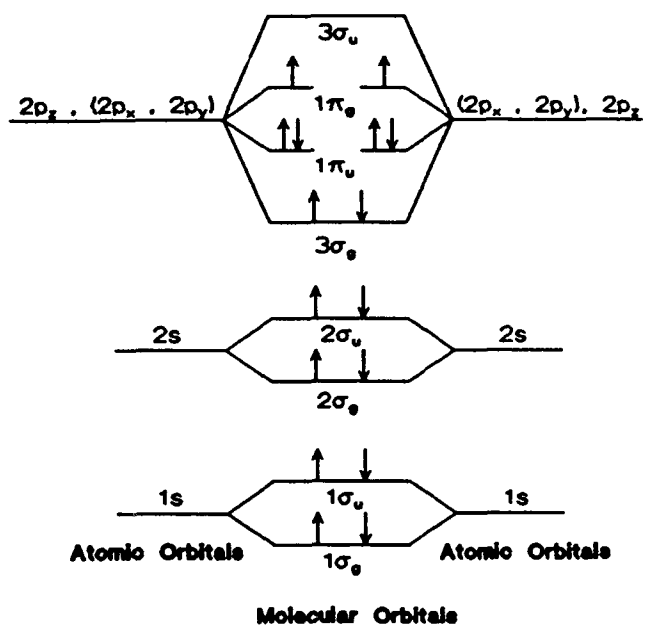
Figure 1. Molecular orbitals for O_2 from linear combinations of atomic orbitals. Arrows indicate occupancy by an electron with $m_s = \pm 1/2$.

$1\pi_g$ Molecular Orbital
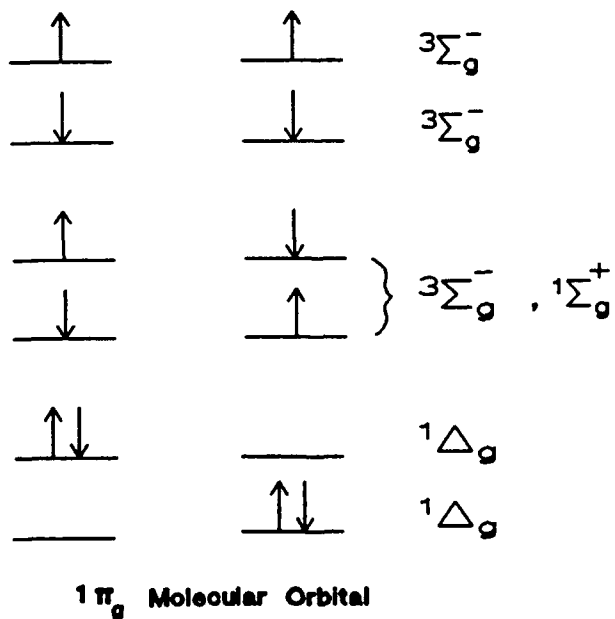
Figure 2. Electronic states for molecular oxygen and the corresponding electronic configuration within the antibonding $1\pi_g$ orbital.

and $b^1\Sigma_g^+$. Potential energy curves for these and higher lying states of diatomic oxygen are shown in Figure 3 (Ref. 13).

Since the three lowest electronic terms of oxygen, X, a, and b, all arise from the same configuration, electric dipole transitions are not allowed between these terms. The O_2(a-X) transition is doubly forbidden (g → g and singlet to triplet transitions are both forbidden for dipole transitions) in the electric dipole since there is no change in inversion symmetry, but a change of one in total spin, and a change of two in total angular momentum. As a result, the radiative lifetime of $O_2(a^1\Delta)$ is ≅ 64 min (Ref. 17). The Einstein A coefficient for the $O_2(a^1\Delta$, v' = 0) to ($X^3\Sigma_g^-$, v" = 0) transition as A_{00} = 2.58 x 10^{-4} 1/s was measured with ≅ 15 percent accuracy (Ref. 17). Radiative lifetimes as long as 90 min have been reported (Ref. 12). Since the radiative lifetime is so long, self absorption effects are negligible for optical path lengths < 100 km (Ref. 10). The first highly allowed electronic transition in oxygen occurs in the ultraviolet between the $B^3\Sigma_u^-$ and $X^3\Sigma_g^-$ states (Ref. 13). The $B^3\Sigma_u^-$ state arises from the molecular orbital configuration 2330 where one electron has been promoted from the $1\pi_u$ bonding orbital to the $1\pi_g$ antibonding orbital.

The O_2(a-X) and O_2(b-X) transitions were recognized early as important atmospheric absorption features (Refs. 18-20). Detailed absorption experiments (Refs. 18-19) have been conducted and Franck-Condon factors reported (Ref. 21). Typical spectra of the O_2(a-X) and (b-X) transitions under moderate resolution are shown in Figure 4 and spectroscopic constants for the X, a, and b states are reported in Table 1 (Ref. 22). Note that the equilibrium internuclear separation is nearly identical for the X and a states. As a result, the (0,0) and (1,1) transitions are highly favored and a large fraction of the total emission from a vibrationally thermalized $O_2(^1\Delta)$ state occurs at 1.268 μm. This lack of dispersion greatly assists in developing emission diagnostics.

Potential energy (eV)

$^1\Sigma_u^+$

$O(^1D) + O(^1S)$

$O(^3P) + O(^1S)$

$^1\Delta_u$

$O(^1D) + O(^1D)$

$O(^3P) + O(^1D)$

21

$B^3\Sigma_u^-$

10

5

$^1\Pi_g$ $^3\Pi_u$ 0 $^5\Pi_g$ $^5\Pi_u$ $^5\Sigma_g^+$ $^5\Sigma_u^-$, $^3\Sigma_u^+$, and $^1\Sigma_g^+$

$^3\Pi_g$ $^5\Delta_g$ and $^5\Sigma_g^+$

O_2

$A^3\Sigma_u^+$ 7   0   5   10 $O(^3P) + O(^3P)$

$c^1\Sigma_u$ $C^3\Delta_u$ $^1\Pi_u$

0     $^2\Pi_u$

$b^1\Sigma_g^+$ 20 $O(^3P) + O^-(^2P^0)$

15

5   10

$a^1\Delta_g$ 0 O_2^-

0   5

$X^3\Sigma_g^-$ 0

0

$X^2\Pi_g$

Estimated error:

——— < 0.02 eV

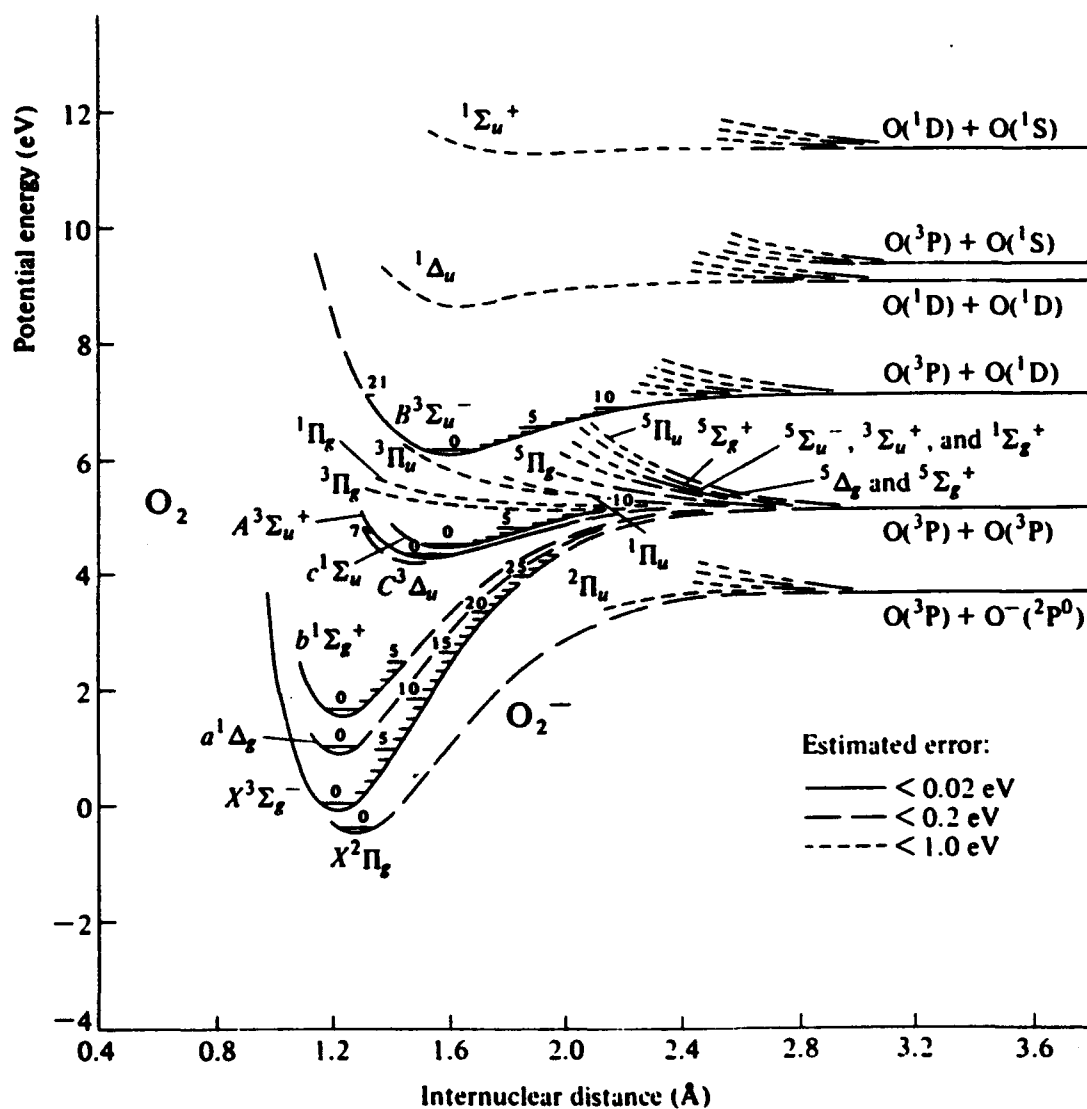— — < 0.2 eV

- - - - < 1.0 eV

Internuclear distance (Å)

Figure 3.   Potential energy curves for molecular oxygen. (From Ref. 7)
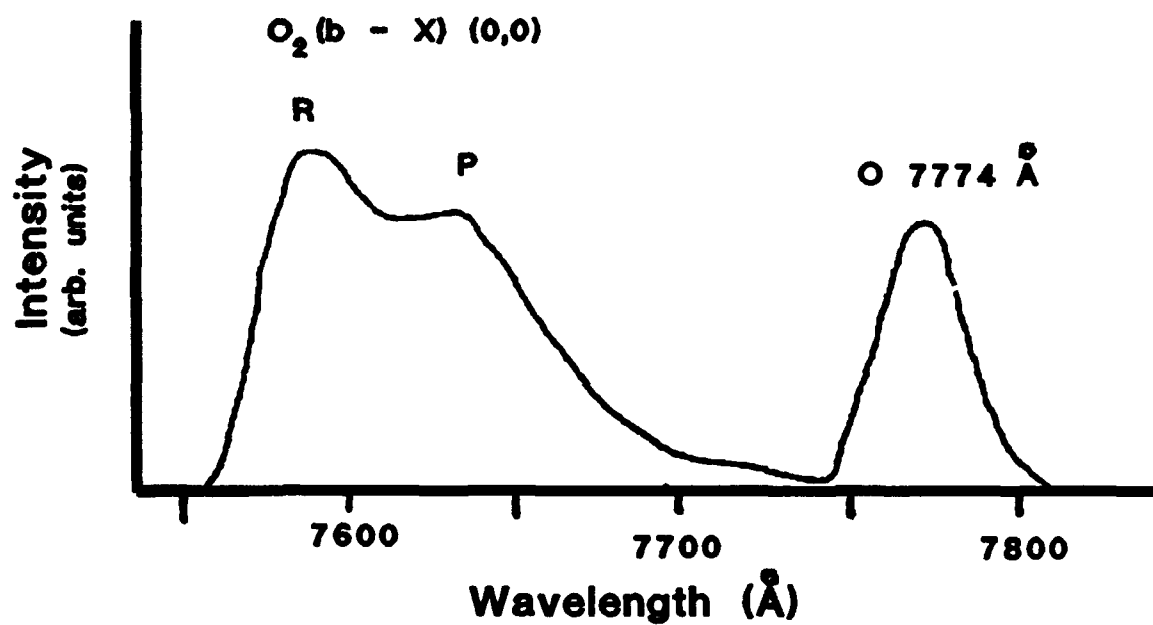
a) Spectrum of O_2(b-X) showing the v' = 0, v" = 0 band.
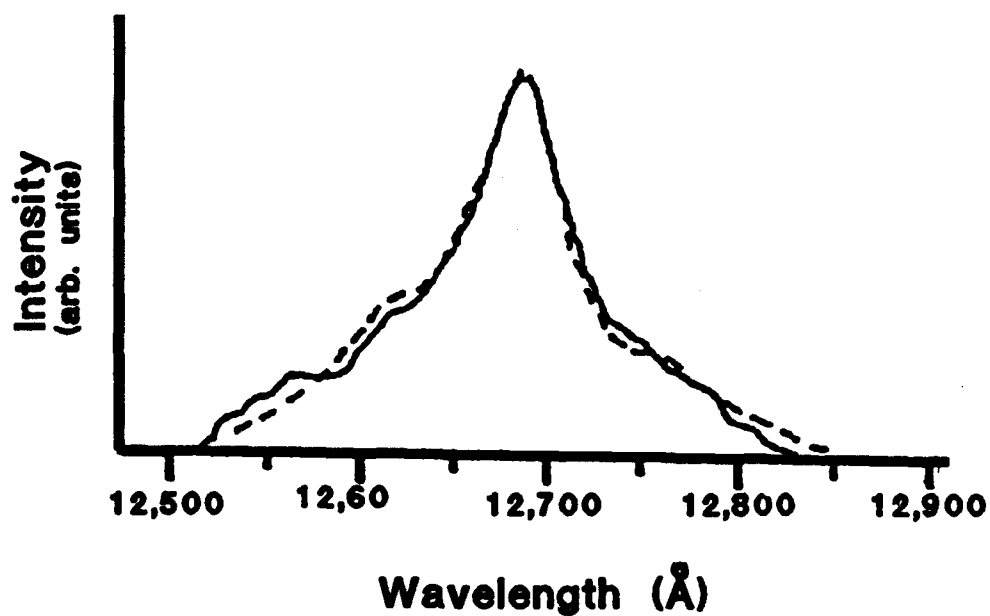
b) Spectrum of O_2(a-X) showing the v' = 0, v" = 0 band.

Figure 4. Low resolution spectra of O_2(a-X) and O_2(b-X). (Ref. 22)

Table 1. Spectroscopic constants for O_2 X, a, and b states.
(All quantities reported in wavenumbers, cm^{-1})

State	T_e	ω_e	$\omega_e x_e$	$\omega_e y_e$	B_e	α_e
$X^3\Sigma_g^-$	0	1580.36	12.073	0.0546	1.44566	0.01579
$a^1\Delta_g$	7918.1	1509.0	12.0	–	1.4264	0.0171
$b^1\Sigma_g^+$	13195.2	1432.687	13.950	-0.01375	1.40041	0.01817

2.2 THE EPR SPECTROSCOPY OF O_2(a) AND O_2(X)

Electron Paramagnetic Resonance or Electron Spin Resonance (ESR) spectroscopy usually refers to microwave transitions between energy levels produced by the application of a magnetic field on an unpaired electron (Refs. 23-24). Unfortunately, the term (EPR) has been applied to magnetically induced transitions which are not necessarily paramagnetic transitions, and the terms EPR and ESR have been used interchangeably. The simplest example of EPR spectroscopy is that of a free electron in the presence of a uniform magnetic field. An electron possesses a magnetic moment, μ, due to its intrinsic spin, $\underline{S}$. This spin may be oriented with or against the applied field, $\underline{H}$, yielding the two spin states denoted by the quantum number, $m_s = \pm 1/2$. The energy degeneracy of these two spin states is removed by the magnetic field. The energy of a magnetic dipole in a magnetic field is given by Equation 1:

$$E = -\underline{\mu} \cdot \underline{H} = \mu_z H = g \mu_B m_s H \qquad (1)$$

where:

μ_z = component of the magnetic dipole in the direction
of the magnetic field

μ_B = Bohr magneton = 9.27×10^{-21} ergs/gauss

g = spectroscopic splitting factor = 2.002

Therefore, the energy difference between the two spin states is

$$\Delta E = h\nu = g\,\mu_B\,H \qquad\qquad (\Delta m_s = 1) \qquad\qquad (2)$$

Under the application of a magnetic field, the electron will undergo a "spin flip" at frequency $\nu = (g\,\mu_B/h)\,H$. The spectroscopic splitting factor is defined as $g = (h/\mu_B)\,d\nu/dH$. Usually the derivative $d\nu/dH$ is a constant. The value of $g\mu_B/h$ for a free electron is 2.8 MHz/G, and thus, for magnetic fields on the order of kilogauss, the transition is in the microwave (gigahertz) region of the electromagnetic spectrum.

A typical EPR spectrometer operates at a fixed microwave frequency, ν, while the magnetic field strength is scanned across the resonance described by Equation 2. When the magnetic field satisfies the resonance condition, the microwave radiation is absorbed by the sample under study and the transmitted intensity decreases. Phase sensitive detection is often employed to improve the detection limits. Figure 5 schematically illustrates the microwave field strength as a function of time. If the modulation amplitude is small compared to the line width, then the derivative of the absorption profile is observed (Ref. 23). Typical EPR signals for a ground state oxygen gas sample are shown in Figure 6.

This simple analysis of EPR spectra applies to gas phase molecules with a single unpaired electron. The EPR spectra can be obtained from other systems. For example, an oxygen molecule has two electrons in the unfilled $1\pi_g$ anti-bonding orbital and its EPR spectrum is more complex. Indeed, for $O_2(a^1\Delta)$, the total electronic spin is zero, and thus, $O_2(a)$ has no spin induced magnetic moment. In addition, a single spin flip in the ground state, $O_2(^3\Sigma)$, involves a change of electronic state (Fig. 2). A more generalized view of angular momentum is required to understand the EPR spectrum of molecular oxygen.

The EPR spectrum for $O_2(a^1\Delta)$ has been analyzed in detail (Refs. 7,9). For the $a^1\Delta$ state of oxygen, the spin angular momentum is zero and for $^{16}O_2$ there is
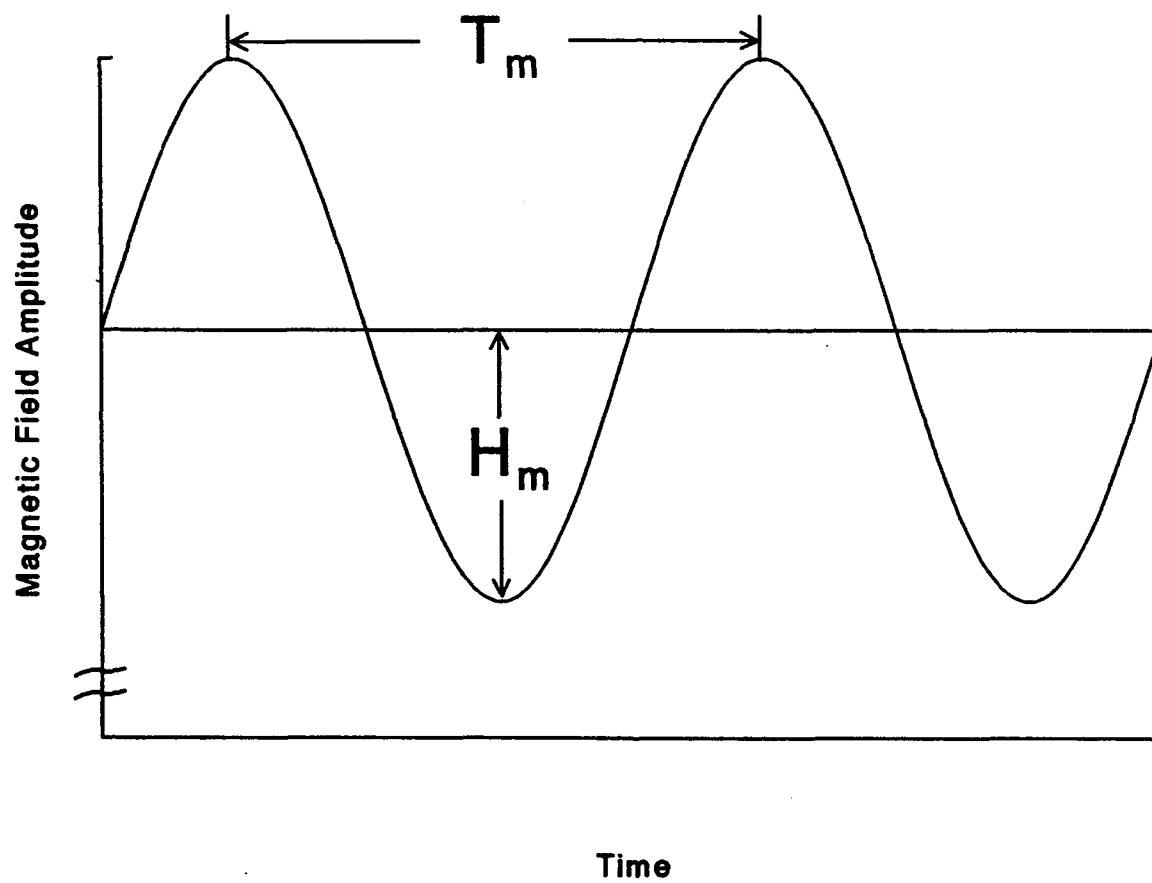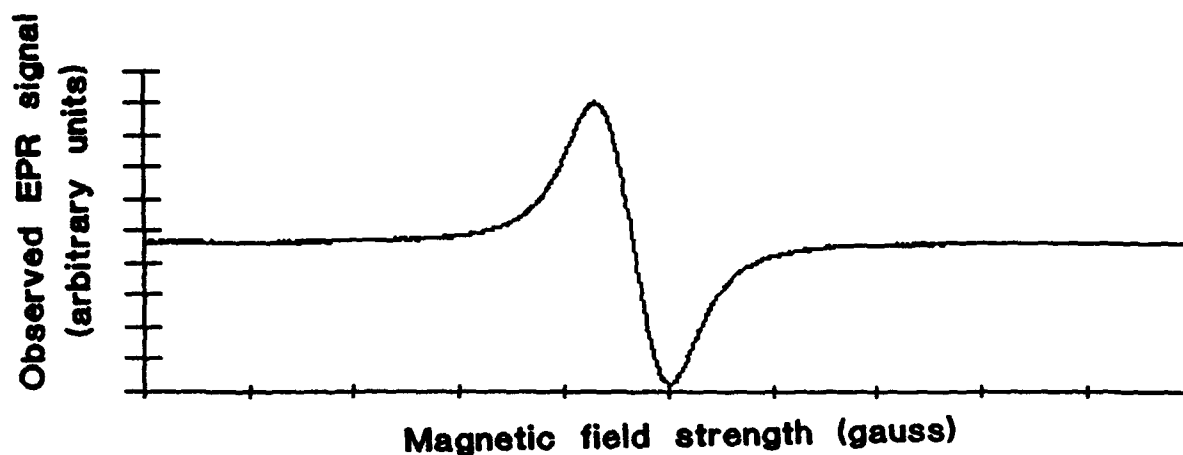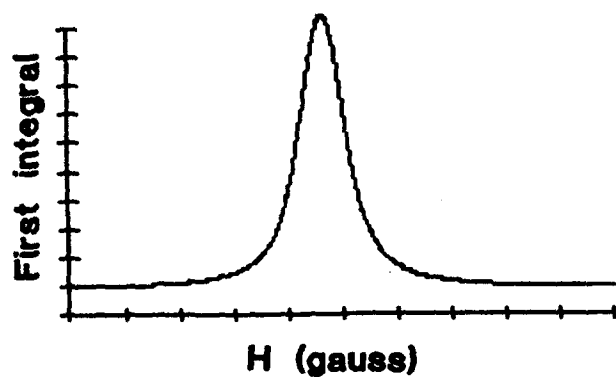
Figure 5. Phase sensitive detection and field modulation parameters.

a) Observed ESR signal showing derivative of absorption feature.

b) First integral of ESR signal showing broadened absorption profile.
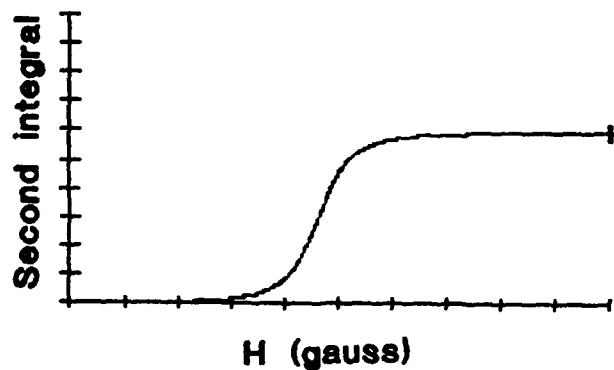
c) Second integral of ESR signal whose asymtope provides area of absorption feature.

Figure 6.   Typical ESR signals observed for ground state molecular oxygen.

11

no nuclear spin. Thus, the total angular momentum, $\underline{J}$, is simply the sum of the orbital angular momentum, $\underline{\Lambda}$, and the rotational angular momentum, $\underline{K}$, so that $\underline{J} = \underline{\Lambda} + \underline{K}$. The orbital angular momentum is related to the magnetic moment by

$$\mu = - g_L \mu_B \Lambda \tag{3}$$

where the spectroscopic splitting factor is $g_L = 1.0$, since only orbital angular momentum is involved. The energy of the magnetic interaction is $E = -\underline{\mu} \cdot \underline{H}$, and for $\Delta M_J = 1$, the energy splitting is

$$\Delta E = g_J \mu_B H \tag{4}$$

where the spectroscopic splitting factor $g_J = \Lambda^2/J(J+1)$ is obtained from the projection of the orbital angular momentum onto the axis of the magnetic field (Ref. 9). The lowest energy angular momentum level of $O_2(^1\Delta)$ is $\Lambda = 2$, $K = 0$ and $J = 2$ which yields a value for g_J of 2/3. For $J = 2$ there are five values for the projection of $\underline{J}$ onto the axis of the magnetic field, $M_J = -2, -1, 0, 1, 2$. According to Equation 4, these states are equally spaced in energy. However, in second order perturbation theory the transition degeneracy is lifted and the energy splittings for $\Delta M_J = 1$ become (Ref. 9)

$$\Delta E = g_J \mu_B H - (2M_J+1) \Lambda^2 g_L^2 \mu_B^2 H^2 / 378B_o \tag{5}$$

where B_o is the rotational spectroscopic constant for the vibrational level $v' = 0$ providing the rotational energy $E_{rot} = B_o J(J+1)$. Figure 7 illustrates the splitting of these M_J levels in the presence of a magnetic field for both the $J = 2$ and $J = 3$ levels of $O_2(a^1\Delta)$. The $J = 3$ level has a degeneracy of $2J+1 = 7$. The rotational energy, $B_o = 1.41808$ cm^{-1} (Ref. 22), is large compared to the magnetic splitting. Using Equation 4, it follows that for a fixed field strength, the splitting between M_J states in the $J = 3$ manifold is smaller than the splitting in the $J = 2$ manifold. To access the transitions in the $J = 3$ manifold using a klystron frequency on the order of 10 GHz, a
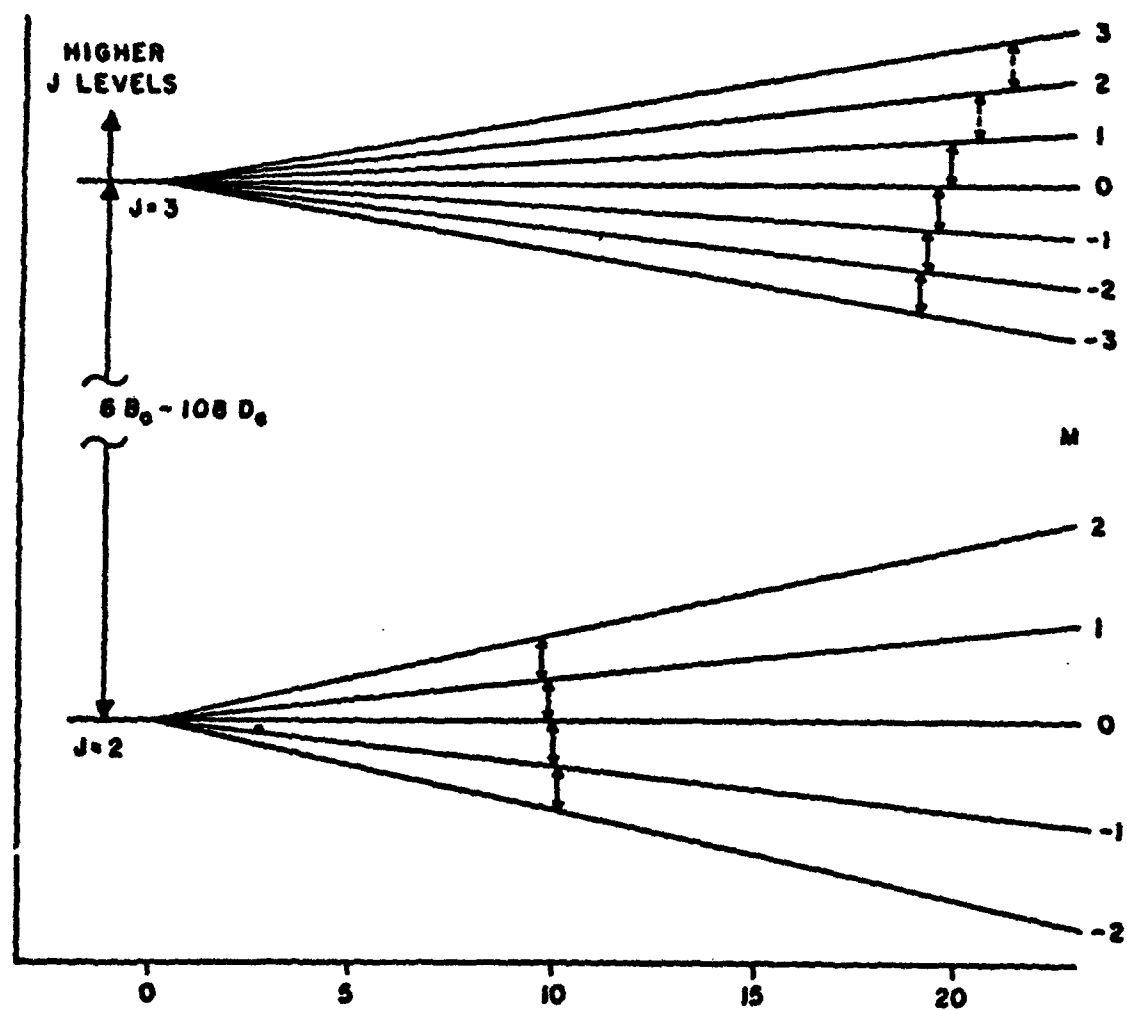
Figure 7. Magnetic splitting of $O_2(a)$ $J = 2$ and $J = 3$ levels. (Ref. 7)

static magnetic field of ≈ 20 KG is needed, which is beyond the capacity of the system used in this study.

The magnetic field strengths experimentally observed by A. M. Falick (Refs. 6,9) for the four $\Delta M_J = 1$ transitions of $J = 2$ at a microwave frequency of 9.29 GHz are reported in Table 2. The observed values for $h\nu/g_J\mu_B H$ may be used to calculate the resonant field strengths at other microwave frequencies from Equation 4. Also listed in Table 2 are the predicted field strengths for the microwave frequency of 8.917 GHz used in the present study.

A more complete solution for the Hamiltonian of a rotating molecule in an external magnetic field may be found in Reference 7. The effect of nuclear spin and a transformation of the Hamiltonian to handle the coupling of different states is presented. The line positions for $O_2(a^1\Delta)$, $J = 2$ and $J = 3$ were observed with considerably greater resolution than in the previous study (Ref. 5) and yield a precise set of rotational and magnetic constants that are entirely self consistent. The improved resolution provided by Reference 7 is not required for the relatively low resolution work to be reported in this document. The relative intensities of the $J = 2$, $\Delta M_J = 1$ transitions have been calculated and are in the ratio 2:3:3:2 for the $M_J = -2$, -1, 0, and $+1$ initial states, respectively (Ref. 9).

The EPR spectrum of ground state oxygen has also been studied in detail (Refs. 5,25). For the $X^3\Sigma_g^-$ electronic state of oxygen, the orbital angular momentum is $\Lambda = 0$, and the total electronic spin is $\Sigma = 1$. Coupling the electronic spin to the molecular rotation, $\underline{K}$, produces the total angular momentum, $\underline{J} = \underline{\Sigma} + \underline{K}$. For $K \geq 1$, each rotational state produces three values of total angular momentum, $J = K + 1$, K, and $K - 1$. The configurations leading to the three triplet spin states are shown in Figure 2. Coupling the magnetic moment of O_2 to an external magnetic field splits the J manifold into 2J+1 nondegenerate states.

14

Table 2. Microwave transitions of O_2(a) in a magnetic field. (Ref. 6)

Transition	Observed Field (Gauss) at ν = 9.29 GHz	$h\nu/\mu_B H$ (observed)	Predicted Field (Gauss) at ν = 8.917 GHz
-2 → -1	10,090.3	0.65596	9,712.6
-1 → 0	9,988.7	0.66264	9,614.7
0 → 1	9,885.6	0.66956	9,515.4
1 → 2	9,781.4	0.67640	9,419.1

The energy of the magnetically split K = 3 rotational level as a function of
magnetic field strength is shown in Figure 8. The J = K ± 1 lines are split
from the J = K lines due to spin-spin interactions of about 60 GHz (Ref. 5).
Spin-orbit and spin-rotation interactions are smaller and split the J = K + 1
and J = K - 1 lines by about -4 to 7 GHz, depending on the rotational state, K
(Ref. 5). A list of observed field strengths for various transitions at a
microwave frequency of 9.000 GHz are provided in Table 3. Also listed are the
relative transition strengths and values for $d\nu/dH$ = $g\mu_B/h$ used to calculate
the resonant field strength, H, for any microwave frequency, ν. Due to spin-
rotational coupling and the large interaction between unpaired electrons in
ground state oxygen, the resonant frequency is not linearly dependent on mag-
netic field. That is, $d\nu/dH$ is not a constant. In addition, the transition
probabilities vary with the frequency. These parameters have been measured as
a function of frequency in the range 8.5 to 9.6 GHz (Refs. 5,25). The line
positions and strengths can be calculated to within ± 2.5 percent (Ref. 5).
The change in $d\nu/dH$ and the transitions probabilities, $|\mu_{ij}|^2$, with frequency
are also given in Table 3.

2.3 RELATIONSHIP OF OBSERVED EPR SIGNALS TO CONCENTRATIONS

Ground state oxygen has often been used as a standard to obtain absolute
concentrations from EPR spectra (Refs. 6,26). Absolute $O_2(a^1\Delta)$ concentration
are obtained by observing the relative EPR signals for $O_2(^1\Delta)$ and $O_2(^3\Sigma)$ in a
pure oxygen flow. Given the total gas pressure, temperature and the ratio,
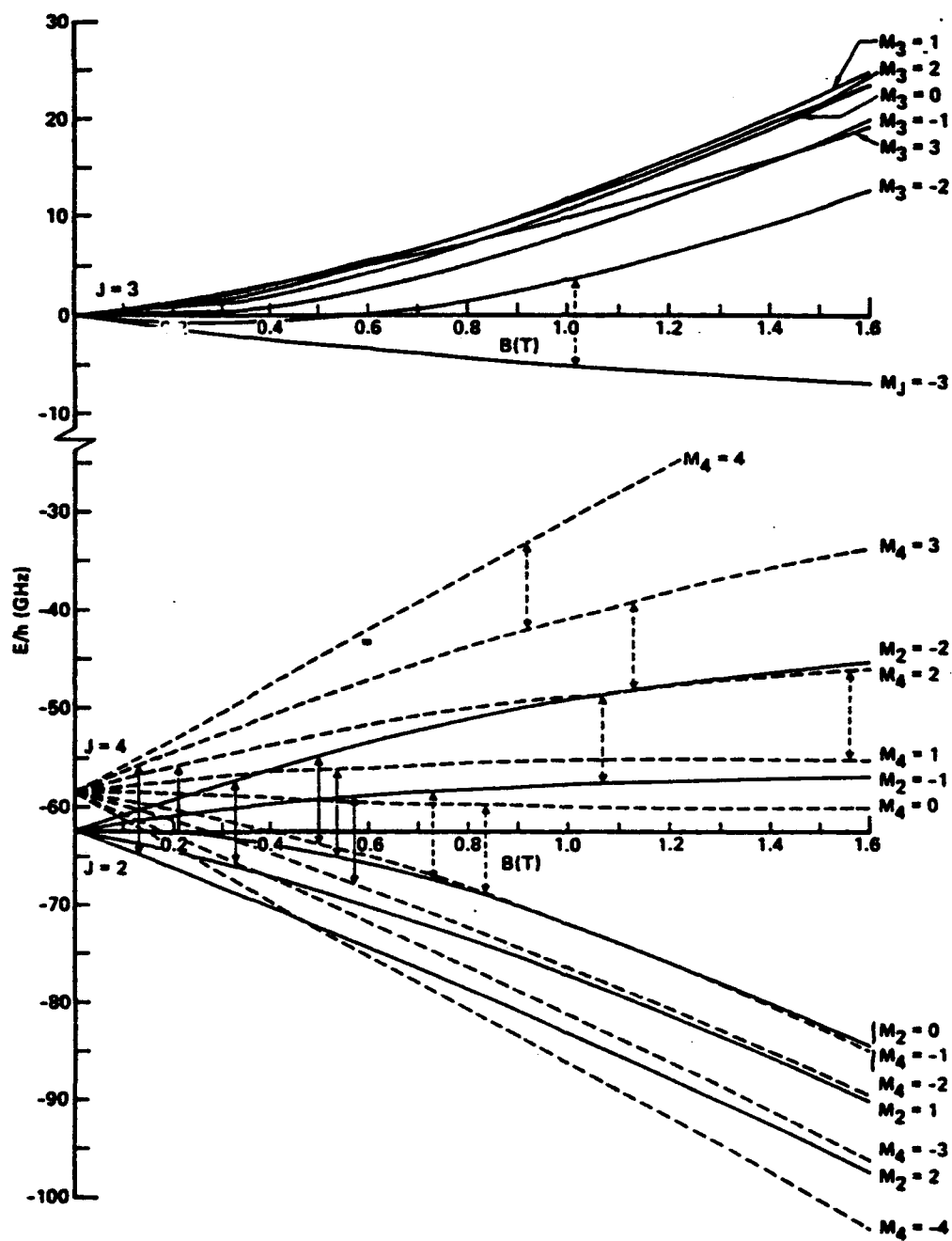
Figure 8. Magnetic splitting of $O_2(X)$ K = 3 rotational states. (Ref. 5)

Table 3. Frequency dependence of transition probabilities for the principal O_2 lines.[a] (Ref. 5)

transition			9.000 GHz			$\Delta(d\nu/dB)$	$\Delta 4[S_x]^2/GHz$
K	J	M	B,[b] Oe	$d\nu/dB$[c]	$4[S_x]^2$	@ $\Delta\nu_o$[d]	@ $\Delta\nu_o$[d]
5	4 → 6	1 → 2	5094	1.817	0.3674	0.045	0.0666
1	1	1 → 0	5343	1.945	0.7354	0.044	0.0241
1	2	1 → 2	5814	1.727	1.2010	0.033	0.0242
1	2	0 → 1	6393	1.429	1.4862	0.000	-0.0021
5	6 → 4	-2 → -1	6237	1.730	0.6265	0.045	0.0725
3	4	-1 → 0	8293	1.660	1.4868	0.076	0.0238
1	2	-1 → 0	6910	1.297	1.2633	0.011	-0.0091
3	4	3 → 4	9242	1.294	0.9217	0.060	0.0431

[a]Calculation valid to ± 1 in last figure for resonant frequency from 8.5 to 9.6 GHz

[b]1 Oe = 0.1 mT

[c]MHz/Oe (1 MHz/Oe = 0.1 GHz/T)

[d]Changes in $d\nu/dB$ and $4[S_x]^2$ per GHz in resonant frequency

$r = [O_2(^1\Delta)]/[O_2(^3\Sigma)]$ and assuming the presence of only $O_2(a)$ and $O_2(X)$ yields the relationships:[*]

$$[N_T] = P/k_BT = [O_2(X)] + [O_2(a)]$$
$$= (1+r) [O_2(X)] \tag{7}$$

$$[O_2(a)] = r/(1+r) (P/k_BT) \tag{8}$$

The extremely small errors associated with assuming only $O_2(a)$ and $O_2(X)$ are present in the flow will be addressed in Section 3.3.

---

[*]Berg, J.O., "EPR Calibration Report", Chemical Oxygen-Iodine Laser Advanced Technology (COIL) USAF Contract No F29601-80-C-0028, 12 April 1982.

The absorbed microwave power is related to the number density of the observed state, with the proportionality constant depending on the transition probability and the statistical population distributions; specifically, the concentration of state i, $[N_i]$, is given by (Ref. 23):

$$[N_i] = (2k_B T/h\nu) \, (\mu_B g_{eff} ZK_i/2|\mu_{ij}|^2) \, I_i \, \exp(-E_i/k_B T) \qquad (9)$$

where:

E_i = energy of state i

Z = molecular partition function

$|\mu_{ij}|$ = transition probability from state i to state j

$g_{eff} = (h/\mu_B) \, d\nu/dH$

K_i = instrument constant, independent of species or state

$I_i = (1/G_i H_m P_\mu^{1/2}) \int_0^\infty \int_0^H \alpha_i' dH' dH$ = integrated EPR signal for state i

$\alpha_i'(H) = d\alpha/dH$ = observed EPR signal for state i

$\alpha_i(H)$ = microwave absorption coefficient for state i

G_i = EPR gain setting for transition (i,j)

H_m = EPR magnetic field modulation amplitude

P_μ = incident microwave power

Thus, the ratio $r = [O_2(a)]/[O_2(X)]$, is simply the ratio of the observed intensities multiplied by a relative intensity factor, $S_{O_2(X)}/S_{O_2(a)}$, and a relative gain setting, $G_{O_2(X)}/G_{O_2(a)}$:

$$r = [O_2(a)]/O_2(X)]$$
$$= (I_{O_2(a)}/I_{O_2(X)}) \, (S_{O_2(X)}/S_{O_2(a)}) \, (G_{O_2(X)}/G_{O_2(a)}) \qquad (10)$$

The relative intensity factor, $S_{O_2(X)}/S_{O_2(a)}$, is a collection of state dependent constants from Equation 9. Based on the reported transition probabilities, the relative intensity factor for the $O_2(a)$ J = 2, M_J = 0 → 1 transition

with respect to the $O_2(X)$ $K = 3$, $J = 4$, $M_J = 3 \to 4$ transition at a microwave frequency of 9.347 GHz and temperature $T = 300$ K has been determined as $(S_{O_2(X)}/S_{O_2(a)}) = 0.624$ (Ref. 4). This value is approximately linearly dependent on temperature due to the partition function (Ref. 5). Due to the nonlinear dependence of the $O_2(X)$ transition probabilities on frequency, this value also depends slightly on frequency. This small frequency effect can be accounted for with the values of $\Delta|\mu_{ij}|/\Delta\nu$ provided in Table 3. The value $(S_{O_2(x)}/S_{O_2(a)}) = 0.624$ is used regardless of microwave frequency.

The broadening of the absorption profile, $\alpha(H)$, can have significant effects on the double integration required to obtain the intensities, I_i. Several mechanisms including collisional relaxation and modulation will broaden the absorption feature. Often, observed profiles exhibit both homogeneous and inhomogeneous behavior. Voight profiles may be used for these convolved cases (Ref. 27). Lorentzian line shapes (characteristic of homogeneous broadening) decay slower than Gaussian line shapes from resonance. (Indicative of inhomo-geneous broadening). A significant error can be obtained when truncating the integration of a Lorentzian profile (Ref. 23). However, correction factors for this truncation can be easily obtained (Ref. 23). The effects of modula-tion broadening and saturation have been analyzed (Refs. 28-32).

2.4 TRANSPORT PROPERTIES OF $O_2(a)$

The design of the calibration setup did not permit the microwave absorption to be measured at the same location as the infrared emission detection. Thus the effects of deactivation during transport of the singlet oxygen must be con-sidered. Equation 22 provides the basis for this correction to the detector calibration, as described in Section 4.0. The efficient transport of singlet oxygen is made possible by both its long radiative lifetime and extremely slow collisional deactivation rates. The gas phase kinetics of singlet oxygen are well known (Ref. 33). There are several paths for energy removal including

radiation, homogeneous gas phase quenching, wall deactivation, and energy pooling:

$$O_2(^1\Delta) \rightarrow O_2(^3\Sigma) + h\nu \tag{11}$$

$$O_2(^1\Delta) + M \rightarrow O_2(^3\Sigma) + M \tag{12}$$

$$O_2(^1\Delta) + O_2(^1\Delta) \rightarrow O_2(^1\Sigma) + O_2(^3\Sigma) \tag{13}$$

$$O_2(^1\Delta) + O_2(^1\Delta) \rightarrow O_2(^1\Delta) + O_2(^3\Sigma) \tag{14}$$

$$O_2(^1\Delta) + O_2(^1\Delta) \rightarrow O_2(^3\Sigma) + O_2(^3\Sigma) \tag{15}$$

$$O_2(^1\Delta) + \text{wall} \rightarrow O_2(^3\Sigma) \tag{16}$$

In addition, the deactivation of $O_2(^1\Sigma)$ can remove energy from the system through the following reactions:

$$O_2(^1\Sigma) \rightarrow O_2(^3\Sigma) + h\nu' \tag{17}$$

$$O_2(^1\Sigma) + M \rightarrow O_2(^1\Delta) + M \tag{18}$$

$$\rightarrow O_2(^3\Sigma) + M \tag{19}$$

$$O_2(^1\Sigma) + \text{wall} \rightarrow O_2(^1\Delta) + M \tag{20}$$

$$\rightarrow O_2(^3\Sigma) + M \tag{21}$$

Deactivation by radiative paths may be neglected due to the extremely long lifetimes of $O_2(a)$ and $O_2(b)$. Recently, Knickelbein and coworkers (Ref. 34) confirmed the long-standing supposition that $O_2(^1\Sigma)$ is quenched to $O_2(^1\Delta)$ rather than to $O_2(^3\Sigma)$. Thus, reactions 19 and 21 may be neglected. An analytical solution for the concentration of singlet oxygen as a function of time can be obtained when the $O_2(^1\Sigma)$ concentration has achieved steady-state conditions (Ref. 35):

$$[O_2(^1\Delta)]^{-1} = \{ [O_2(^1\Delta)]_o^{-1} + A/B \} \exp(Bt) - A/B \tag{22}$$

where:

$[O_2(^1\Delta)]$ = concentration of $O_2(^1\Delta)$

$[O_2(^1\Delta)]_0$ = concentration of $O_2(\Delta)$ at t = 0

$$A = k_{13} + k_{14} + k_{15}$$

$$B = k_{16} + k_{12}[M]$$

$$[O_2(^1\Sigma)] = k_{13} [O_2(^1\Delta)]^2 / (k_{20} + k_{18}[M])$$

[M] = concentration of arbitrary quencher; predominantly water and $O_2(X)$

The steady-state condition for singlet-sigma oxygen is attained rapidly. Note that the relative importance of quenching (Equation 12) and pooling (Equation 13) depends critically on the excited oxygen yield. In typical flow tube experiments quenching dominates the deactivation, whereas pooling dominates under laser device conditions.

In the development of chemical generators of singlet oxygen a correlation between singlet oxygen concentration and total pressure, partial pressure of singlet oxygen, temperature and total flow rate has been developed and termed the "chi correlation" (Ref. 12). This relationship includes only second order kinetic deactivation and should not be applied to microwave sources of singlet oxygen where the yield is low and ground state oxygen quenching of $O_2(a)$ is important.

3.0 EXPERIMENTAL APPROACH

3.1 CALIBRATION APPARATUS

A schematic of the experimental apparatus for calibrating the infrared emission detector using EPR spectroscopy is shown in Figure 9. The apparatus consisted of four major subsystems: (1) a flow tube and source of singlet oxygen, (2) an optical collection system and infrared detector, (3) an EPR spectrometer, and (4) a data acquisition system. Each of these subsystems will be described in detail, followed by a discussion of important design issues.

A moderate gas velocity (900-4500 cm/s) flow tube was designed to generate and transport a laminar flow of singlet and ground state oxygen to a calibration volume where the emission from $O_2(a)$ was detected and to the cavity of an EPR spectrometer where the relative $O_2(a)$ and $O_2(X)$ concentrations were observed. A Kinney model 850 mechanical vacuum pump (800 CFM) assisted by a Roots model MF2700 blower (2400 CFM) was used to establish a flow rate of 50 to 1000 sccm of pure oxygen controlled by a Unit Instruments model URS 100-5 mass flow controller with a model UFC 1000 sensor operating in the range of 0 to 2000 sccm. Pressures as low as 17 mtorr and leak rates < 40 mtorr/min were achieved. Pressures in the range of 50 to 1500 mtorr were recorded with MKS model 390HA 1-torr and model 122AA 10-torr capacitance manometers calibrated for zero, linearity and span on a MKS model PVS-2A-0100 with 270B signal conditioner calibration stand. A linear regression analysis provided a slope of 1.0020 and an intercept of 0.002. Pressure readings were accurate to within 0.5 percent. A manifold was constructed to sample the pressure at each of eight different locations with the same sensor. The zero calibration of the pressure transducer was checked regularly on a 2-in oil diffusion pump.

Total flow rates were measured and actively controlled by the controller operating in the range of 0 to 2000 sccm. The manufacturer's calibration for nitrogen gas was corrected for oxygen flow by the square root of the ratio of heat capacities, $\sqrt{C_p(O_2)/C_p(N_2)} = 0.996$. The gas temperature was measured with Medtherm type T gas phase thermocouples to an accuracy of $\pm 0.1°C$. The
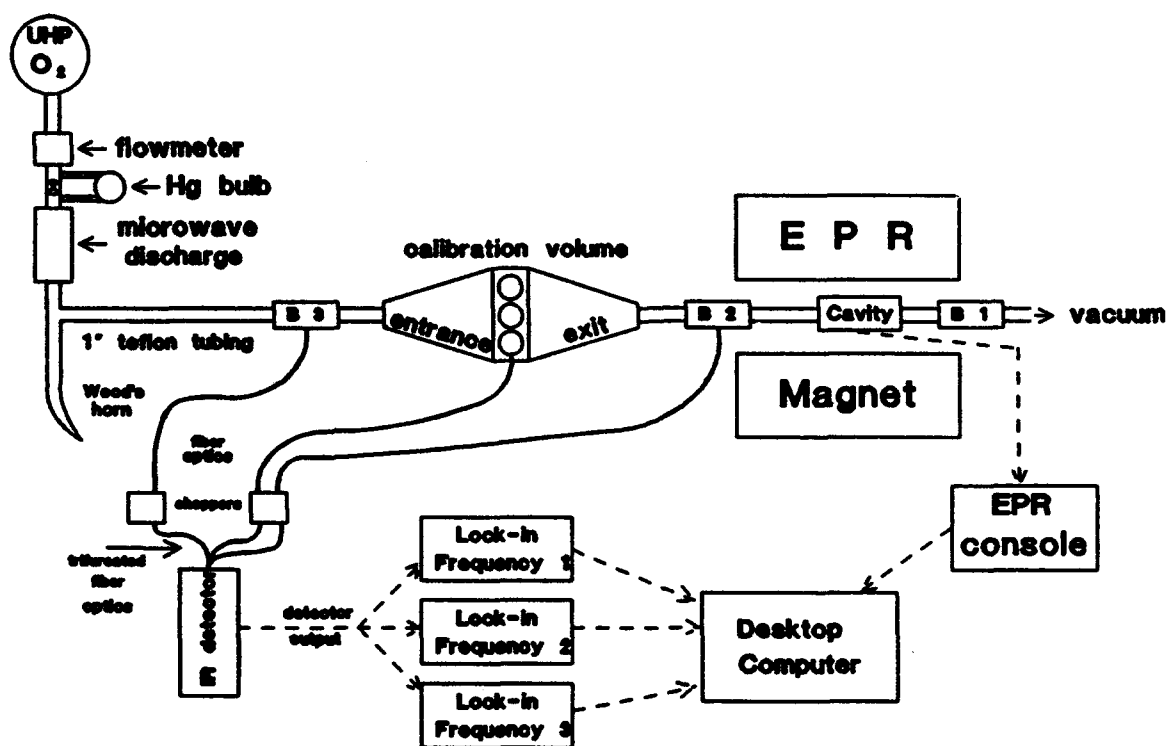
Figure 9. Schematic diagram of $O_2(a)$ detector calibration apparatus.

temperature did not depend on flow conditions or microwave power and the room temperature was maintained at a constant 21 °C. The measured flowing gas temperature was always T = 21 ± 1 °C. The locations for pressure, temperature and mass flow measurements are indicated in Figure 10.

Ultra-high purity oxygen was passed through a Opthos Instruments gas nitrogen cooled Evanson microwave cavity via 1.27-cm diam quartz tubing to generate 5 to 14 percent $O_2(a^1\Delta)$. The cavity was excited by a Kiva model MPG-4 2480- MHz magnetron generator with 70 W forward and 1 to 2 W reflected power. A Wood's horn situated just downstream of the microwave cavity was used to reduce the scattering of the microwave generated emission.

The reaction $O + NO \rightarrow NO_2 + h\nu$ leads to broad band (visible and IR) emission. The emission is within the 1.27 μm band pass of the detector and can cause calibration errors.[*] The microwave cavity produces both oxygen and nitrogen atoms. To eliminate oxygen atoms, a mercury oxide coating was applied to the walls of the microwave exit channel to induce oxygen atom recombination. This method has been used by several research groups (Refs. 37, 39). Air leaks upstream of the microwave cavity are the only source of nitrogen. There were no air leaks detected upstream of the microwave discharge with the leak detector used in this work. Consequently, no recombination emission was observed under visual inspection. A more detailed analysis of this emission intensity is provided in Section 3.3.

The oxygen was transported to the calibration volume through 2.21-cm inner diameter Pyrex tubing. One of three optical detection blocks (Fig. 11) was connected to the Pyrex tubing with Nacom 2.54-cm diam Teflon fittings to monitor the concentration of $O_2(a^1\Delta)$ delivered by the microwave generator. Two additional detection blocks, B1 and B2, upstream and downstream of the EPR cavity were used to monitor singlet oxygen deactivation. To maintain laminar flow and prevent axial pressure gradients, entrance ramps with an expansion

---

[*] Ibid, pg 17.
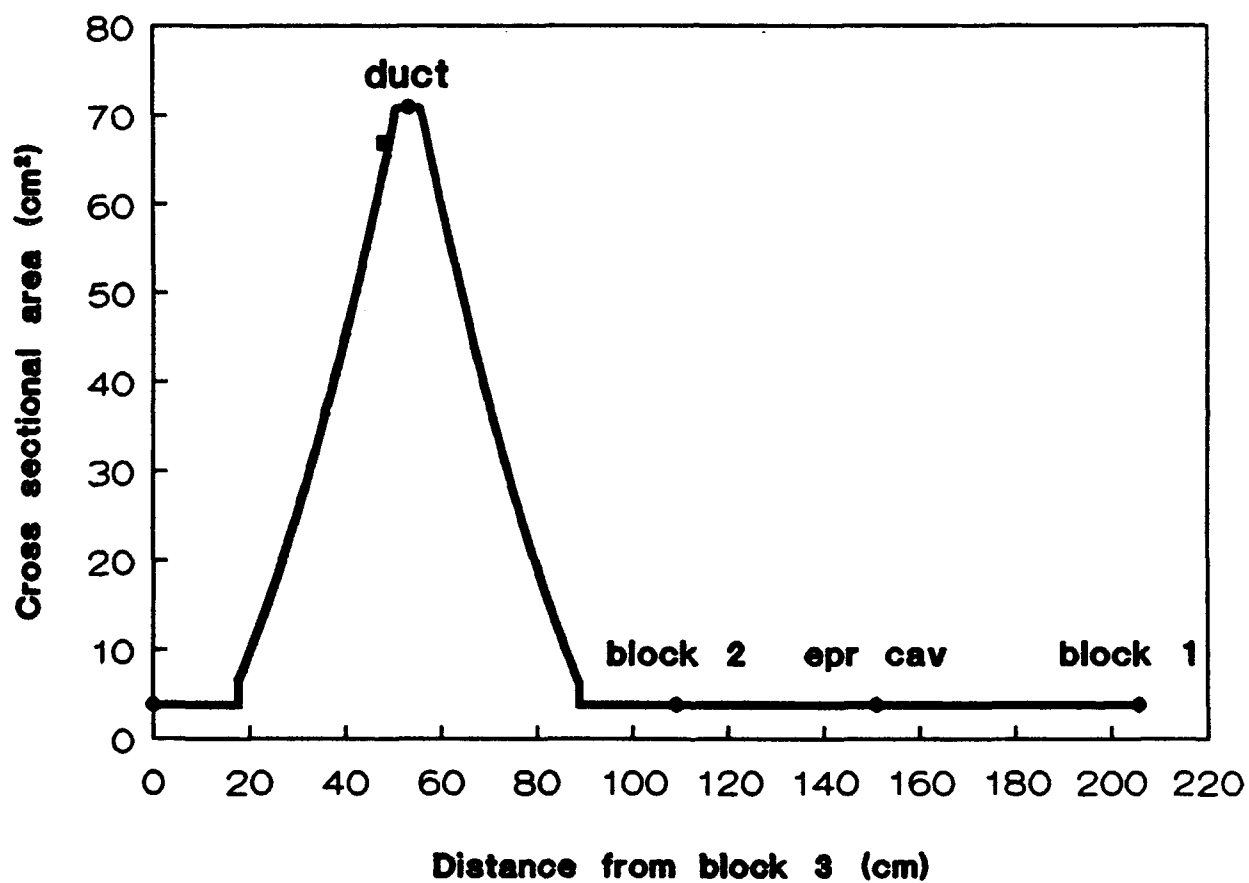
Figure 10.   Cross sectional flow area versus downstream position,
             measured from block 3.   Locations of temperature (■)
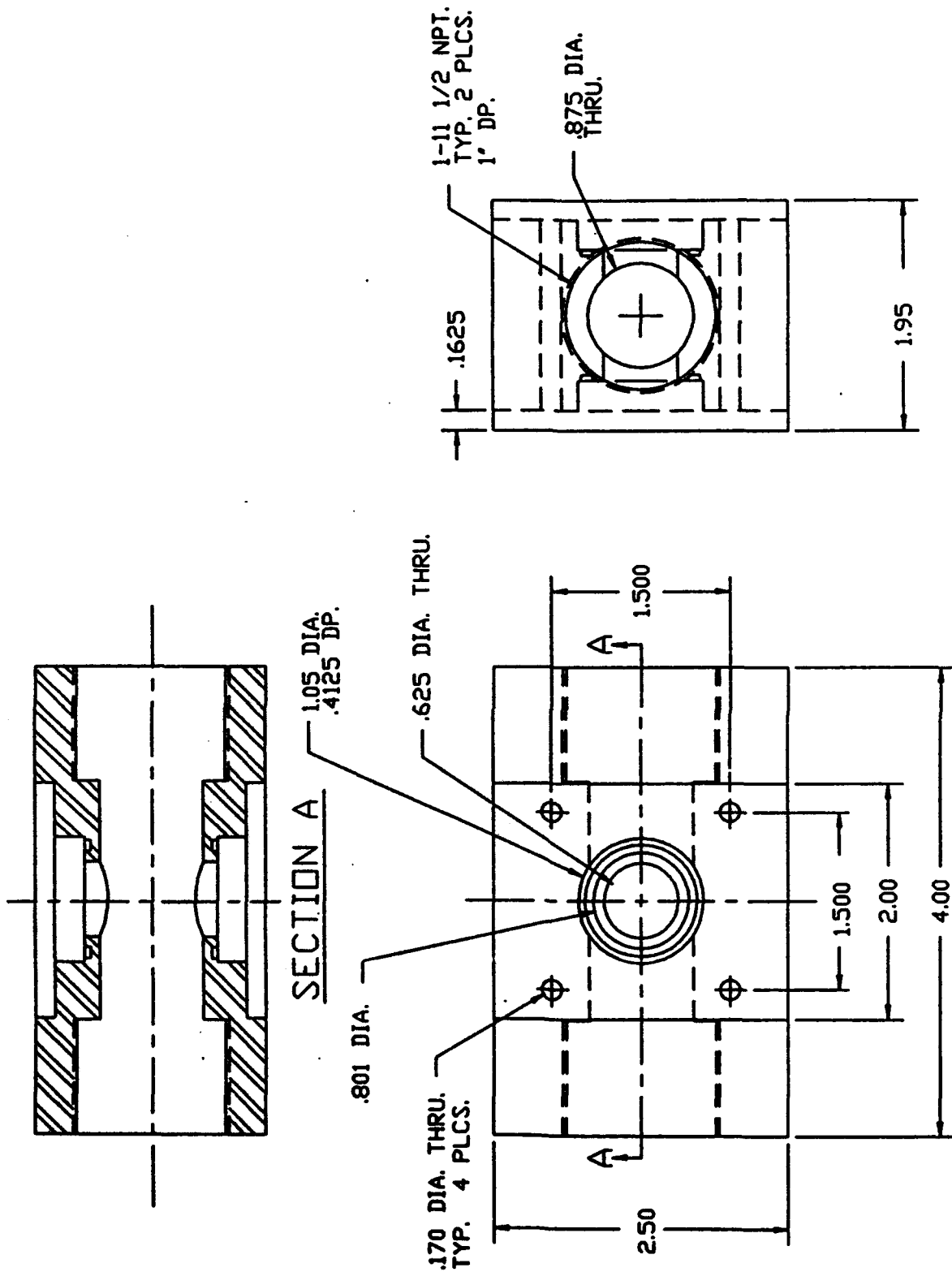   and pressure (·) measurements are also indicated.

Figure 11. Drawing of optical detection block.

half-angle of 12° were designed to transition the flow from the 1-in diam
tubing to the 17.8- by 4.0-cm cross section of the calibration volume. The
interior of the entrance ramps and calibration duct were coated with identical
black Kynar material used in the diagnostic duct of the COIL device (this
material is used on COIL to reduce wall deactivation of singlet oxygen).
Thus, any differences in light scattering between the calibration duct and
the COIL device were eliminated.

It was possible to detect the $\lambda = 1.268$ μm emission from $O_2(a\Delta, v' = 0)$ to
$O_2(X^3\Sigma, v'' = 0)$ at any of the three detector blocks (B1, B2, B3) or any of
the three windows in the viewing volume hardware. The optical collection
system included an Oriel quartz $f = 75$ mm collimating lens with a limiting
aperture of 1.07 cm. The emission from the collimated viewing volume was
focused onto the end of an Oriel 3-mm diam by 9.1-m long glass fiber optic
bundle for transmission to the detector assembly. According to the manufac-
turer the fiber optic introduced an optical loss of ~ 3 percent per meter at
$\lambda = 1.268$ μm. To reduce the sensitivity of the detection system to changes in
collection efficiency, transmission, optical focus, and geometry, the complete
optical and detector system was designed as a single unit, as shown in Figure
12. An interference filter centered at $\lambda = 1.268$ μm with a full-width at
half maximum of 10 nm was used to limit the the detected emission to the
single vibrational transition of $O_2(a^1\Delta, v' = 0)$ to $O_2(X^3\Sigma, v'' = 0)$. The
average transmission of the filter was 26.4 percent for the $v' = 0$, $v'' = 0$
transition. The detector housing could accommodate neutral density filters to
attenuate signals incident at the detector. The optic probe mount included a
shutter to eliminate all light incident on the detector when necessary. The
output from the fiber optic bundle was focused with a $f = 75$ mm lens to over-
fill the active area (25 mm^2) of the IR detector.

A liquid nitrogen (LN_2) cooled intrinsic germanium detector manufactured by
the Applied Detector Corporation, model 403L, was used to detect the infrared
emission. The radiant flux incident on the detector due to the $O_2(a)$ emission
for a concentration of 10^{14} molecules per cubic centimeter was calculated to
be $\approx 10^{-12}$ W. This detector has a large responsivity, R $= 7 \times 10^9$ V/W, and

DC output → DVM

AC output → Lock-in

Germanium detector

Detector housing block

Nitrogen gas purge

Bandpass filter

Flange Connector Ring

2 in. filter holder

1 in. filter adapter

Neutral density filters

optic probe mount

focusing optic probe with shutter

Glass fiber optical cable

Collimating optic probe

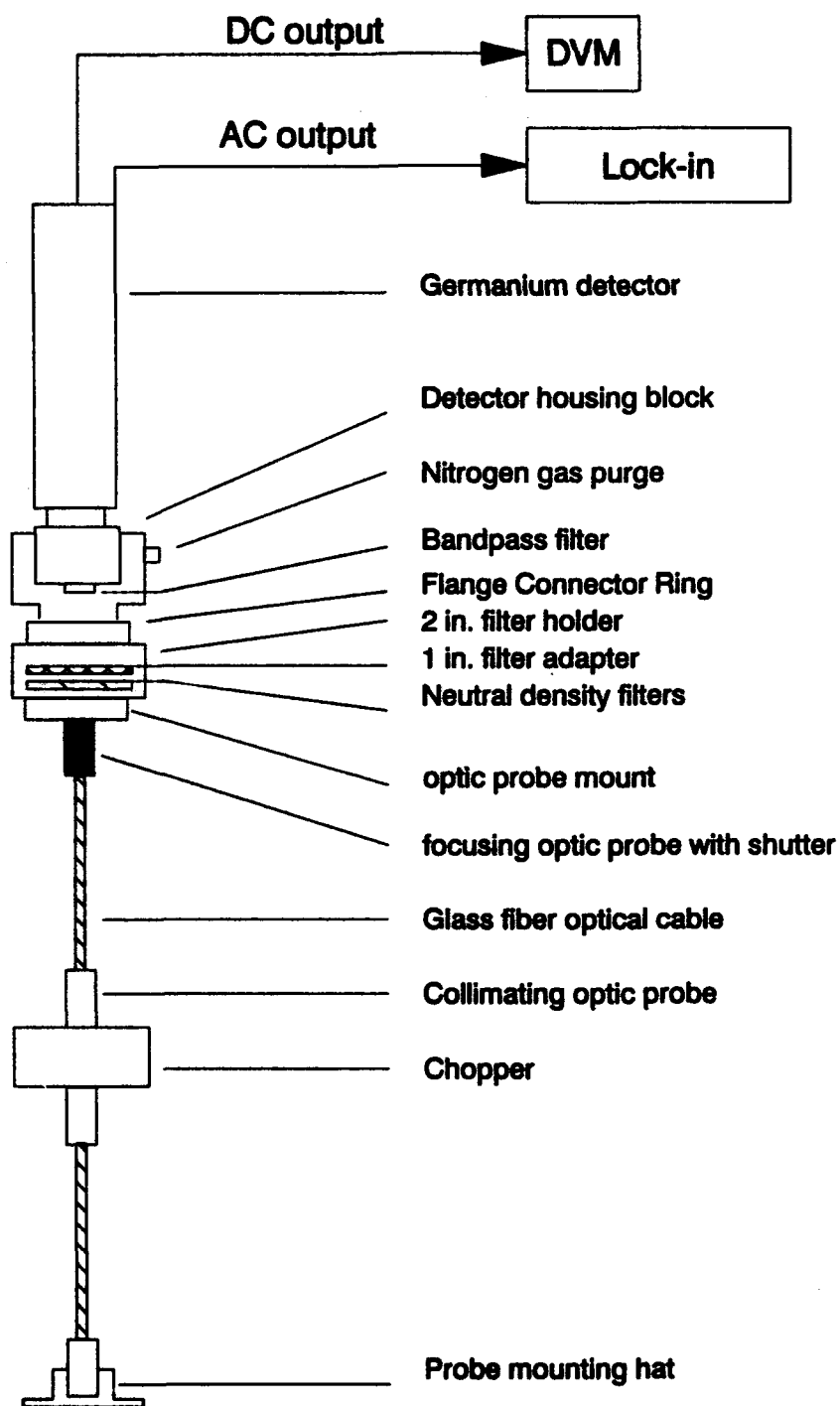Chopper

Probe mounting hat

Figure 12.   Schematic diagram of $O_2(a)$ optical detection system.

moderate noise equivalent power, NEP $\approx$ 8.6 x 10^{-16} W, so that the detectivity is large, D^{*} = 5 x 10^{+12} m-Hz$^{1/2}$/W. The active area of the detector is 25 mm^{2} and has a linear response in the chopper frequency range 10 to 500 Hz. The responsivity peaks at 1.6 μm and drops by $\approx$ 60 percent at 1.268 μm.

The detector required a power supply (ADC model PS-1 or PS-2) operating at -250 VDC. The detector DC output voltage served two functions: indicating proper operating temperature and optical saturation of the detector. When cooled to 77 K the detector output DC voltage read -1.25 V. A DC voltage near 9 V indicated optical saturation. The detector signal due to background light was undetectable with a dark signal of $\approx$ 50 μV. Further characterization of the detector is provided in Section 3.3.

A single IR detector was used to record up to three different emission signals by chopping the light at three different frequencies and using a trifurcated fiber optical bundle to couple the emission to the detector's active area. Phase sensitive detection was used to increase the detection limit and signal to noise ratio. Two PAR model 192 dual-frequency mechanical choppers provided the distinct frequencies of 94.33, 79.39, and 55.55 Hz. The detector's AC output voltage was processed by Ithaco model 395 Heterodyne Narrowband Volt-meters with auto-phasing capability. Typical signals ranged from 0.3 to 2 mV for a time constant of 0.3 s.

A Varian E-Line model E-112 Electron Paramagnetic Resonance Spectrometer (Ref. 40) was used to measure the relative O_2(a) and O_2(X) concentrations. A Varian V-7300-12 in electromagnet established a variable magnetic field strength of 0 to 10,000 G. The magnet was driven by a V-7700 5-to 90-A 13-kW power supply. The magnetic field was modulated at 100 kHz with a peak-to-peak amplitude of 0.5 to 4.0 G by an E-207 High Frequency module. A model E-102 Microwave Bridge with Klystron was the source of the X-band microwave radia-tion with a frequency of 8.8 to 9.6 GHz and a maximum power of 200 mW. A rectangular cross section waveguide with a 60-dB variable attenuator was used to transport the microwave radiation to the model E-231 cavity. The rectangu-lar TE$_{102}$ cavity provided an unloaded quality of Q = 7000. Typically, the EPR

spectrometer was operated at the fixed microwave frequency 8.92 GHz while the magnetic field strength was scanned by 20 or 40 G over either the $O_2(X^3\Sigma)$ K = 3, J = 4, M_J = 3 → 4 transition at 9171 G or the $O_2(a^1\Delta)$ J = 2, M_J = 0 → 1 transition at 9515 G. A gain of 250 for $O_2(X)$ and of 3200 for $O_2(a)$ were typically used to provide measured signal to noise ratios of 500:1 and 100:1, respectively. The detected EPR signal, the derivative of the absorption as a function of magnetic field $\alpha'(H)$, was recorded on an E-200A oscilloscope, E-080A X-Y plotter, and the computer data acquisition system A typical 40 G scan required 2 min for $O_2(^1\Delta)$ and 1 min for $O_2(^3\Sigma)$.

The calibration data were acquired and stored on a Zenith Z-248 personal computer system for further data analysis. Pressure, temperature, mass flow rate, IR detector signals at each of three locations (B2, Calibration Volume, and B3), and $\alpha'(H)$ were recorded using the ASYST laboratory software package. Data were acquired at a rate of 1000 points per scan. A series of data files for various pressures, flow rates, $O_2(a)$ microwave powers, and EPR spectro-meter settings were obtained for each detector calibration. The first and second integrals of the observed EPR signal, $\alpha'(H)$, were computed and dis-played. The areas were obtained using a Simpson integrating routine after subtraction of the baseline. The baseline was calculated as an average of all the $\alpha'(H)$ data points, as suggested in Reference 23.

3.2 CALIBRATION PHILOSOPHY

To improve the calibration's validity, every attempt was made to make the calibration conditions as similar as possible to those expected on the COIL where the detector was to be used. The detector was calibrated on a flow apparatus with identical viewing volume, reflective surfaces, viewing windows, etc. as the COIL diagnostic duct. This eliminated potential problems of viewing volume differences between the calibration duct and the COIL duct.

For large viewing volumes, it may be impractical to calibrate the detector on an exact replica of the laser hardware. Large volumes imply long transport times and greater deactivation of the singlet oxygen. As a result, the signal

to noise ratio of the $O_2(a)$ EPR signal was substantially reduced and the required correction for deactivation is large and uncertain. Indeed, these errors exceed those caused by transferring the calibration to different viewing volumes. The error analysis presented in Section 5.0 provides the basis for assessing the relative importance of these various sources of error and selecting a best calibration approach for a given situation.

A detector assembly was designed and fabricated as a single unit to reduce the sensitivity of the detection system to changes in collection efficiency, transmission, optical focus, and apparatus geometry. Once assembled, the detection system remained intact.

A series of at least 10 calibrations was performed on five IR detectors using the apparatus and procedures described in this document during the period from September 1985 to December 1988. This extensive set of data provided a unique opportunity to assess the reproducibility and long term stability of the calibrations. A complete history of the calibrations and data for the application of this diagnostic on a high power COIL device will be forthcoming.[*] The importance of multiple calibrations and regular detector sensitivity tests to assess changes in diagnostic performance with time cannot be overemphasized.

3.3 CHARACTERIZATION OF CALIBRATION SYSTEM

A detailed assessment of the operating characteristics of the calibration apparatus is absolutely necessary to assess systematic and statistical errors associated with the final detector calibration factor. A characterization of the four subsystems: (1) flow tube and microwave source of singlet oxygen, (2) optical collection system and infrared detector, (3) EPR spectrometer, and (4) a data acquisition system is provided in the following paragraphs. With careful experimental procedures, the system can be characterized with great accuracy.

---

[*] To be published as a Phillips Laboratory technical report.

3.3.1 Flow Tube and $O_2(a)$ Source

The fully developed, laminar flow in a circular tube of constant area is described as Hagen-Pousille flow (Ref. 41). The mean velocity for such a flow is

$$v = -(1/8\mu) \, r_o^2 \, dP/dx \tag{23}$$

where:

r_o = the radius of the tube

μ = the gas viscosity

dP/dx = the pressure gradient in the flow direction

From mass continuity, $\dot{m} = \rho v A$, the total flow rate is

$$\dot{m} = -(P\pi r_o^4/8\mu k_B T) \, dP/dx \tag{24}$$

If the driving force ΔP is proportional to the head pressure, then the mass flow rate will depend quadratically on pressure. Figure 13 illustrates the observed flow rates for pressures of 0.1 to 10 torr for blocks 1 and 2. Figure 13b shows data for pressure up to 1 torr, the range used during the calibrations. Indeed, the plots of flow versus pressure squared are extremely linear in this pressure range with correlations of $r = 0.9992$ and 0.9997 for blocks 1 and 2, respectively. The slopes for a given block are different for the low and high pressure ranges. For example, the slope in the low pressure region for block 1 is 673.0 sccm/(torr)^2 as compared to a slope of 594.1 sccm/(torr)^2 for the full pressure range, about 12 percent lower. Similarly, the slopes in the low and high pressure regions for block 2 are 1126.4 sccm/(torr)^2 and 937.1 sccm/(torr)^2, respectively, with the latter being 17 percent smaller. The differences in slope for a given block are possibly due to a nonlinear response of the vacuum station or hysteresis in the mass flow controller. A small, positive intercept in flow rate equal to 44.6 ± 0.1 sccm is observed at both blocks. This intercept is attributed to a zero offset in the mass flow controller, with further justification provided below. Due to
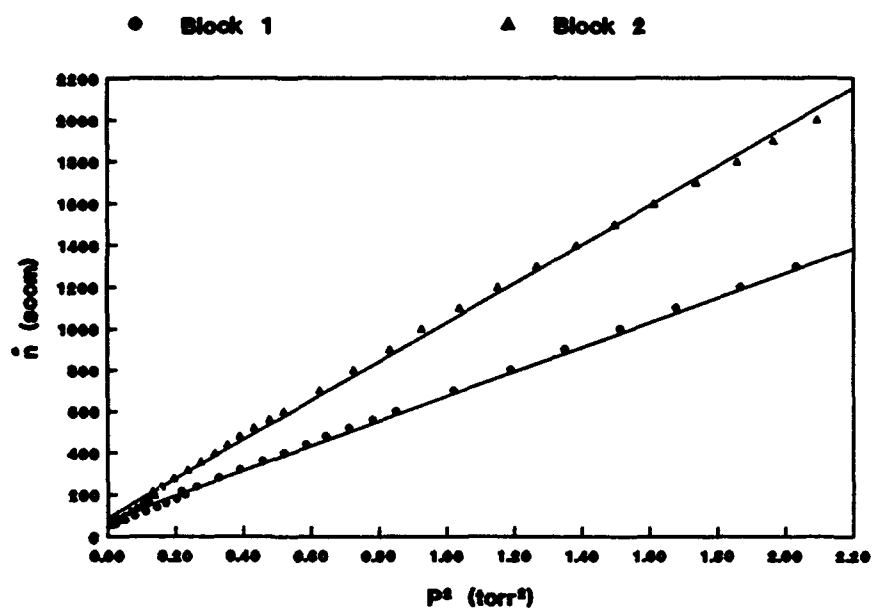
a) High pressure
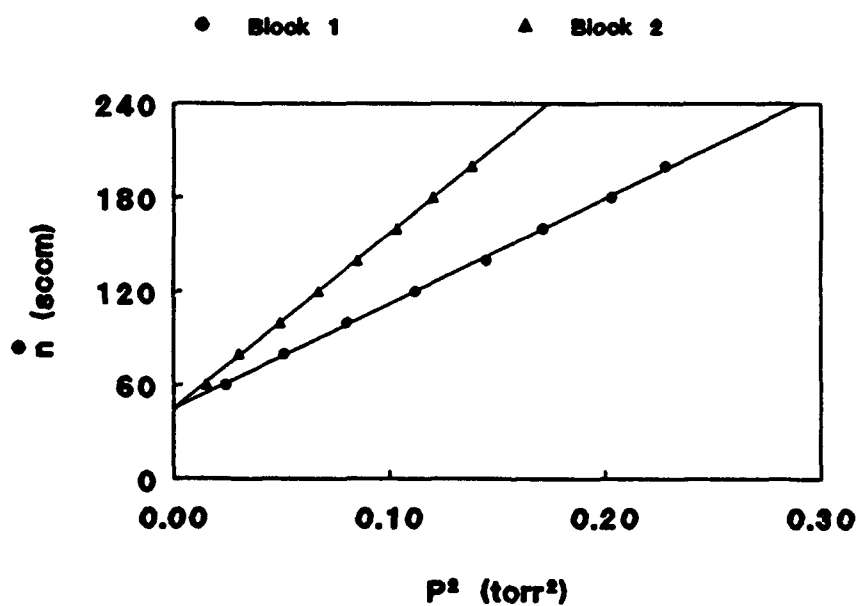
b) Low pressure

Figure 13. Pump curve: flow rate as a function of pressure.

frictional losses, the pressure decreases as a function of distance down the flow tube according to

$$P_2^2 - P_1^2 = (16\mu k_B T/\pi r_o^4) \ (\dot{m}/m) \ (x_1 - x_2) \tag{25}$$

This equation is obtained by solving Equation 24 for PdP and integrating over a distance $x_2 - x_1$ for a constant temperature T. Figure 14 demonstrates that the observed pressure drop between the two optical detection blocks B1 and B2 obeys Equation 25. Figures 13 and 14 provide a good system check for the calibration of the capacitance manometers and flow meters. The fitted intercept of Figure 13 agrees favorably with that of Figure 14. The predicted slope of Figure 14 from Equation 25, 1656 ± 59 sccm/torr^2, agrees favorably with the measured value, 1620 ± 7 sccm/torr^2. The uncertainty in the predicted slope arises primarily from the error in determining the tube radius, r_o. An absolute error of <0.1 mm provides a 3 percent uncertainty due to the fourth power dependence. Thus, any systematic error in pressure or flow rate other than the mass flow offset already identified must be < 4 percent, and is more likely < 1 percent. It is also demonstrated that Equation 25 can be used to extrapolate between the two pressure readings at B1 and B2 to obtain the pressure in the EPR cavity. The EPR cavity pressure is required to evaluate the relative $O_2(a)$ to $O_2(X)$ concentration from Equation 8.

Since the flow rate is quadratically dependent on pressure, the velocity must be linearly dependent on pressure. The Mach number M = v/a, where a = 465.5 m/s is the speed of sound in oxygen at T = 300 K, is linearly dependent on pressure as shown in the plot of Figure 15. The data have been corrected for a mass flow controller offset of 44.6 sccm and that successfully brings the data to a zero intercept. The Mach number is low, M ≤ 0.10, and the fluid is incompressible. This characterization of the flow velocity will be required to calculate transport times and correct for the deactivation of singlet oxygen, as described in Section 4.0.

Characterization of the flow in the calibration volume is complicated by the variation of cross-sectional area with flow distance. The area profile for the flow tube is shown in Figure 10. The observed pressures in the diagnostic
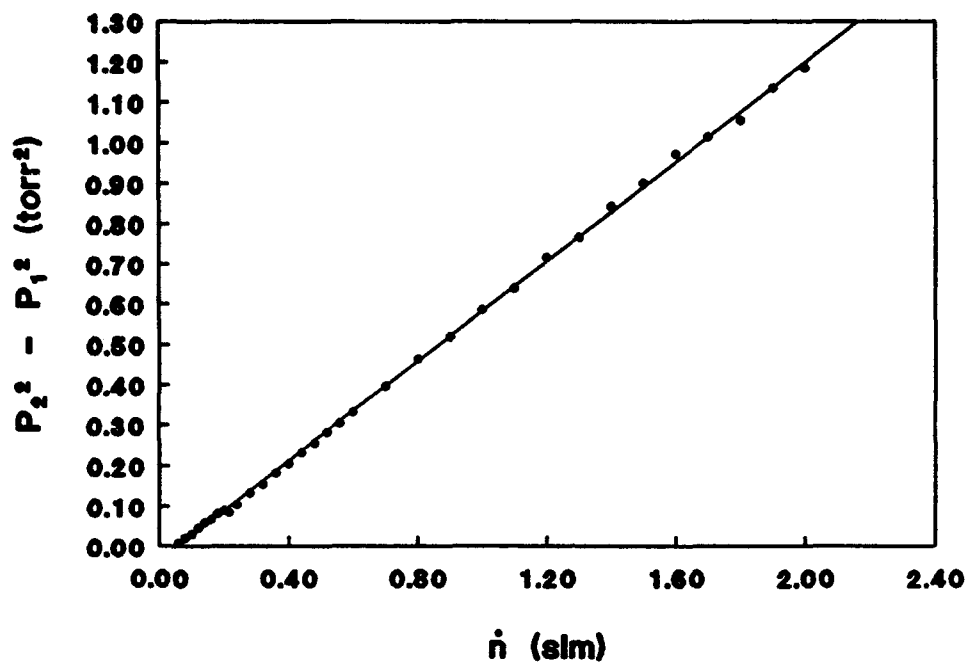
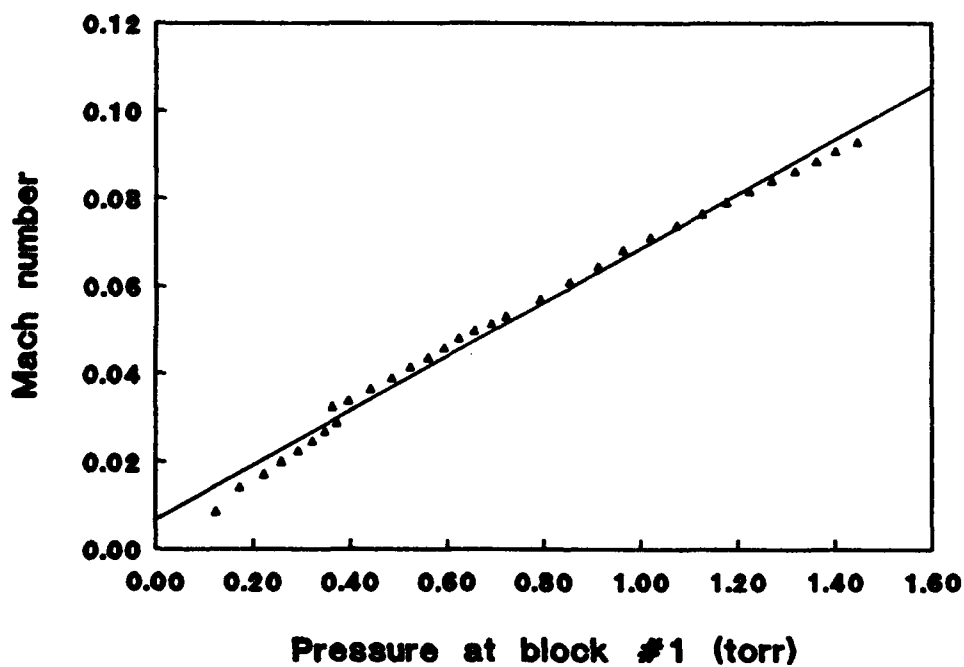Figure 14. Friction losses as a function of flow rate.

Figure 15. Mach number as a function of pressure.

duct as well as the pressures at B1, B2, and B3 for various flow rates are shown in Figure 16. The predicted pressures based on a one dimensional aero-kinetic model, DEACT (Ref. 42), are also shown in Figure 16. The observed pressures agree favorably with the computational predictions and this computer model will be used in Section 4.0 to assess the extent of singlet oxygen deactivation.

The velocity changes with the cross-sectional area to conserve mass flow according to Equation 26,

$$V(x) = \dot{m}/\rho A(x) = \dot{m} \ (k_B T/P) \ / \ A(x) \tag{26}$$

Thus, the variation of velocity with flow distance, x, can be obtained for any flow condition from the data presented in Figures 10 and 16.

A check for any radial variation in pressure across the flow in the diagnostic duct was performed by measuring the pressure at the center of the flow and at the side wall. No difference in pressure was observed over a wide range in flow rates. The sensitivity of this test was better than 0.2 percent. Thus, no problems with nonuniform flow fields or "jet-streaming" were encountered.

The efficiency of the microwave generator at producing $O_2(^1\Delta)$ decreased at increased cavity pressures, as shown in Figure 17. These data were acquired over several different test days. Absolute concentrations were obtained from the detector calibration reported in Section 4.0. The scatter in the data is relatively large, $\pm$ 15 percent. This scatter is due to both the lack of reproducibility of $O_2(a)$ EPR absorption areas and the sensitivity of the EPR microwave generator to cavity tuning. Also, no attempt was made during the calibration to reproduce a given yield (as might be done by reproducing flow and pressure conditions and setting the forward and reverse powers of the microwave power supply).

Also shown in Figure 17 are the $O_2(a)$ generation efficiencies observed by other researchers. It is quite typical to obtain 5 to 15 percent of $O_2(a)$ in
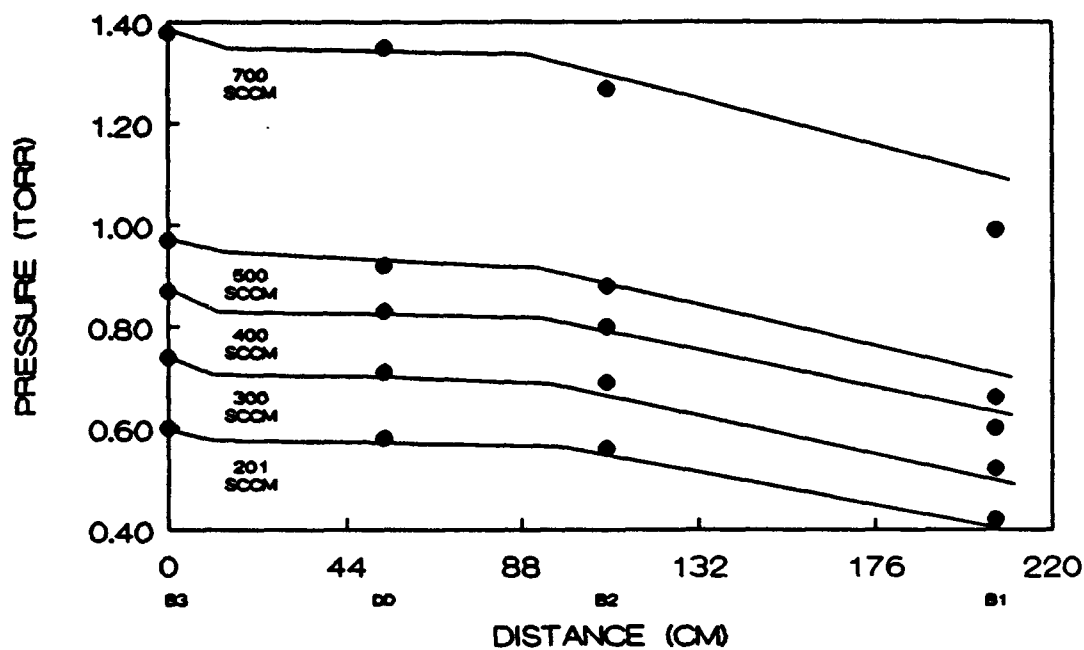
Figure 16. Pressure profile in the flow direction within the calibration
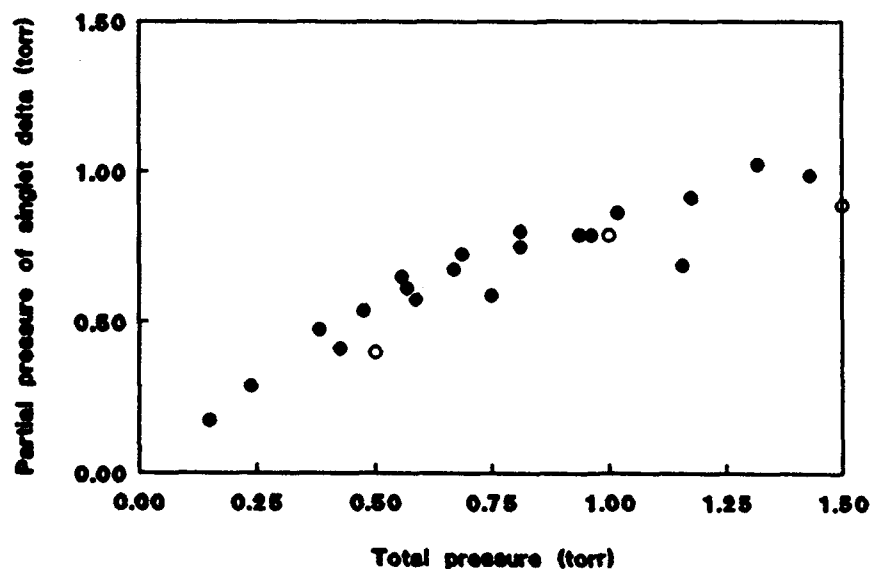duct. (·) observed data, (——) DEACT model predictions.

Figure 17. Efficiency of the microwave generator at producing singlet
oxygen. (●) data from the current study, (o) data from
Reference 8.

such microwave systems (Refs. 4,8). Such a limitation provides a quick check on the magnitude of any calibration. Note that the partial pressure of $O_2(a)$ continuously increases with pressure at least to 1.5 torr total O_2 pressure. The microwave source for $O_2(a^1\Delta)$ is extremely stable. The IR signal was observed by the Wang detector over a period of 16 min. No long term change in the signal is observed and noise fluctuations are < 0.5 percent. This result implies that the both the $O_2(^1\Delta)$ and $O_2(^3\Sigma)$ flows remain constant during the time required to obtain their EPR spectra. Although the stability of a standard microwave generator may be good, one must be rather cautious in calibrating a detector of singlet oxygen solely on its reported performance and efficiency, as has been suggested (Ref. 4).

The emission resulting from NO + O recombination is broad band and partially overlaps the narrow $O_2(a-X)$ emission at 1.25 to 1.29 μm. By using two narrow band-pass filters at 1.268 $\pm$ 0.010 μm and 1.3152 $\pm$ 0.010 μm, the ratio of the observed intensities for NO + O and $O_2(a-X)$ emission may be experimentally determined. The NO + O emission at 1.3152 μm was undetectable under typical operating conditions and a massive air leak was introduced for these tests. For an air flow rate upstream of the microwave generator of ≈ 600 sccm and a total pressure of 1 torr, a green emission was visually observed in a darkened room and a 0.3 mV signal recorded at 1.315 μm on the IR detector. The artificial leak rate is 10^3 to 10^4 times larger than the apparatus leak rate. Most of the apparatus leak rate occurs downstream of the microwave discharge. Thus, an upper bound to the NO + O signal under typical operating conditions is 0.3 μV, which is 100 times smaller than the detector dark signal.

In the absence of a mercury coating on the exit walls of the discharge tube, oxygen atoms were detected at the EPR cavity. With small amounts of mercury (Hg) applied to the walls, the oxygen atom concentration was reduced by 50 percent, and with moderate mercury coating no oxygen atoms were detected at the EPR cavity.

3.3.2 Optical Collection and Detection

The IR emission detection system including detector and electronics exhibits a highly linear response to incident intensity, as shown in Figure 18. The emission from a blackbody source was transmitted to the collimating lens, fiber optic, and germanium detector through an interchangeable neutral density filter and the resultant AC signal was recorded on the lock-in amplifier. The observed signals range from 0.2 to 300 mV and are nearly linear over the full range with a correlation of > 0.9994. Thus, the EPR calibration can be extrapolated to considerably larger $O_2(a)$ concentrations with high confidence. Note that with the calibration factor presented in Section 4.0, the 300 mV signal corresponds to an $O_2(a)$ concentration of 12.7 torr.

The data presented in Figure 18 determine the relative calibration of the two different IR detectors. The relative slopes are equal to the relative calibrations as follows:

$$CAL_1/CAL_2 = slope_1/slope_2 \tag{27}$$

where:

$slope_i$ = slope for detector i

CAL_i = calibration factor for detector i, as defined in Equation 27

The ratio CAL_1/CAL_2 is determined to within 2 percent and is considerably more accurate than any absolute calibration. This result can be used to further constrain the error of two independent, absolute calibrations and to transfer a known calibration from one detector to a second.

The IR detector response is strongly dependent on chopping frequency. The temporal response of the ADC model 403L germanium detector is relatively slow (10 ms). The ADC detector responds to light modulated in the range of 0.5 to 500 Hz. The frequency stability of the mechanical light choppers was within ± 0.2 percent.
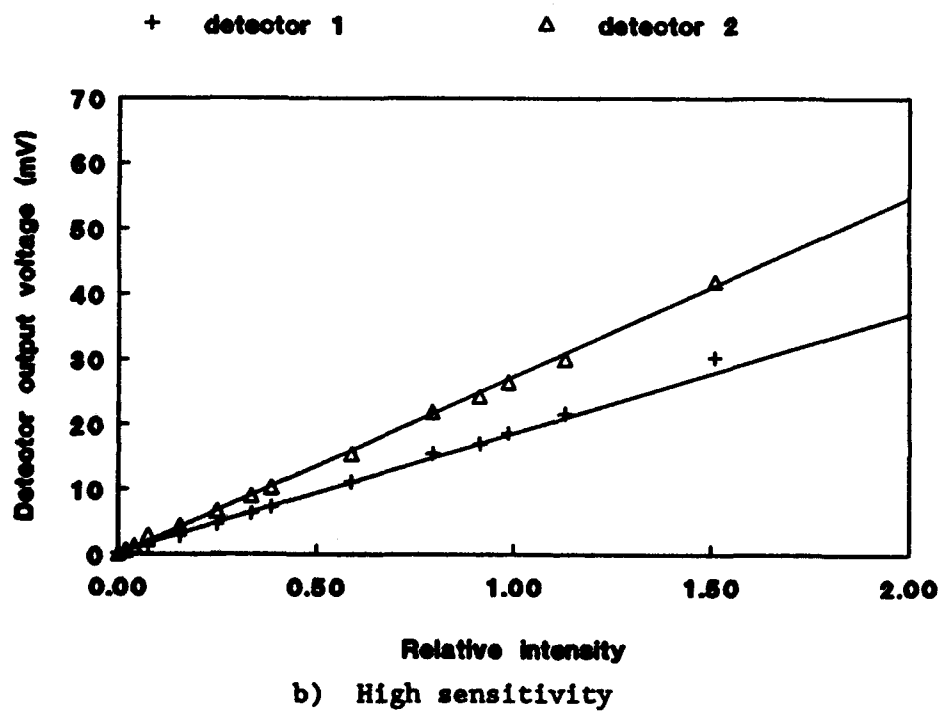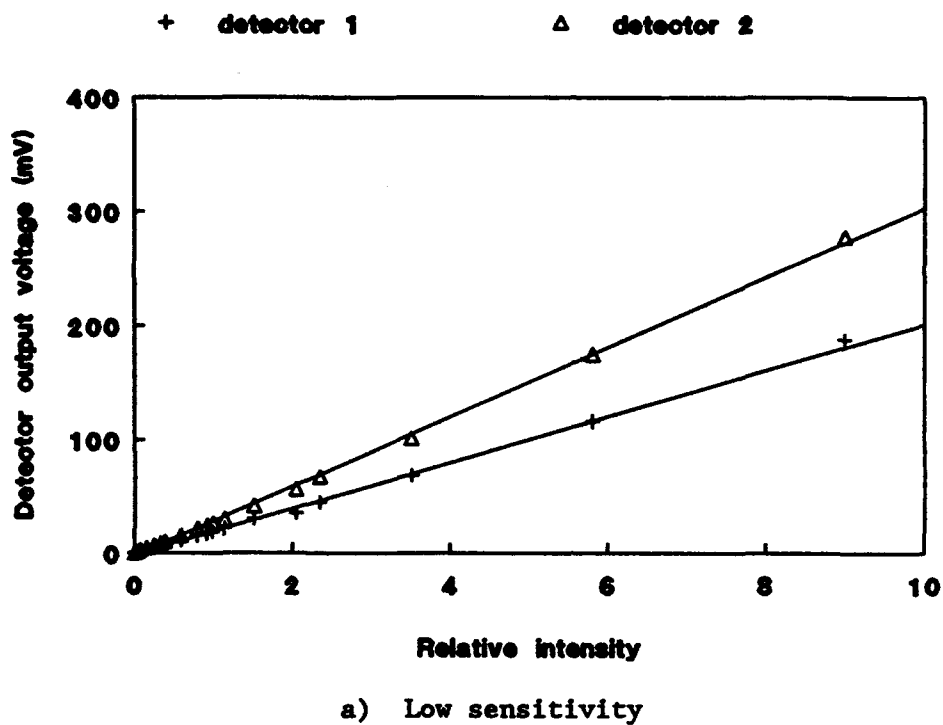
a) Low sensitivity

b) High sensitivity

Figure 18. Linearity of IR detection system.

Characterizing the collimation length of the optical collection system is a difficult task. Several qualitative checks were performed to assess the sensitivity of the calibration to viewing volume. First, the collection optic was moved away from the fixed calibration duct along the optical axis by 0 to 2 cm and no change in signal was observed. Second, the O_2(a-X) emission was observed at both detection blocks B3 and B2 (path length 2.21 cm) and at the calibration duct (path length 3.99 cm). Comparisons between the signals at B3, B2 and at the duct were made. Corrections for the path lengths and the pressure drops were made, and an independent estimate of the deactivation was provided by DEACT code (Section 4.0). The values measured for O_2(a-X) at B3 and the corrected value at the duct agreed to within 2 percent. Similar results were obtained for the values at the duct and B2. Finally, a large path length correction of 4.8 was successfully applied to actual COIL hardware between the oxygen generator and the diagnostic duct. Thus, viewing volume corrections based on relative optical path lengths is viable for volume ratios of 2 to 5. It is still highly desirable to calibrate on an exact volume replica of the intended laser hardware for the best calibrations.

3.3.3 The EPR Spectrometer

The EPR spectrometer's signal to noise characteristic was measured with a standard pitch sample (Ref. 40). The noise trace was obtained with no pitch sample in the cavity. The signal to noise ratio obtained from the measured spectrum is 445:1, in good agreement with the instrumental specification of 500:1.

The $O_2(X^3\Sigma_g^-)$ K = 3, J = 4, M_J = 3 → 4 transition at H = 9188 G was used for the calibration reference in the present study. The spectrum is dense below ≈ 9000 G and no attempt to assign these transitions was made.

A complete EPR spectrum of $O_2(a^1\Delta)$ J = 2 is shown in Figure 19. The four ΔM_J = 1 transitions are indicated and are separated by 97 to 94 G. The relative intensities are in the proportion 2.09 : 3.11 : 2.99 : 1.91, in good agreement with theory. The strong feature at H = 9673 G is due to the $O_2(X^3\Sigma)$
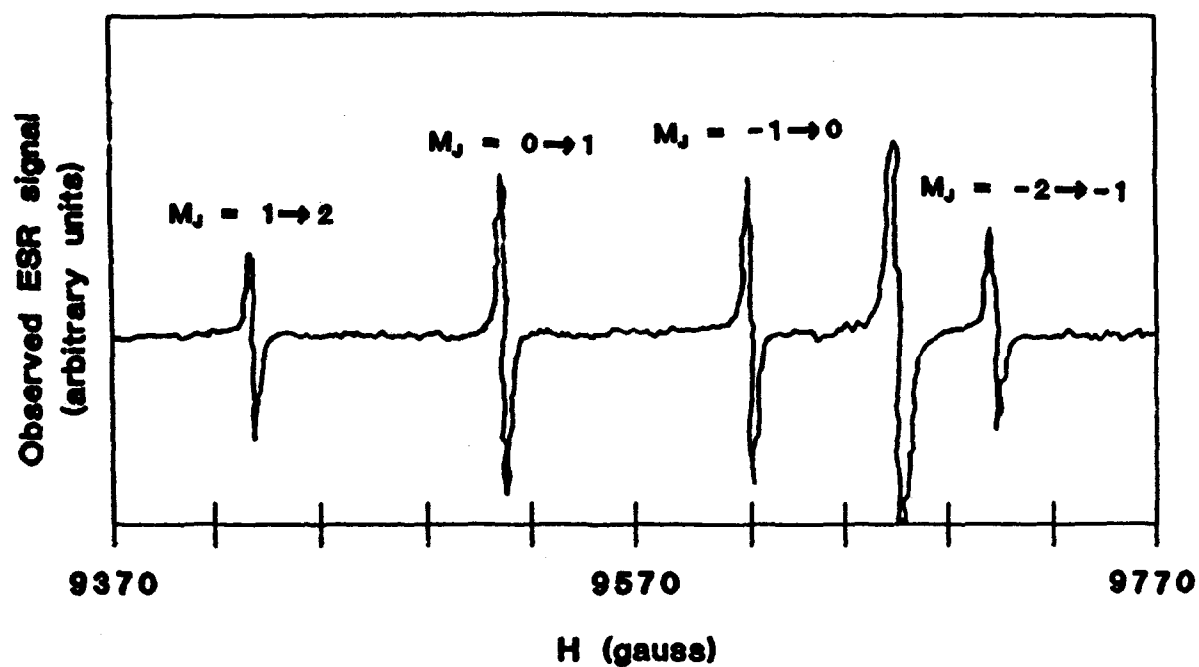
a) Observed ESR signal of $O_2(a)$.
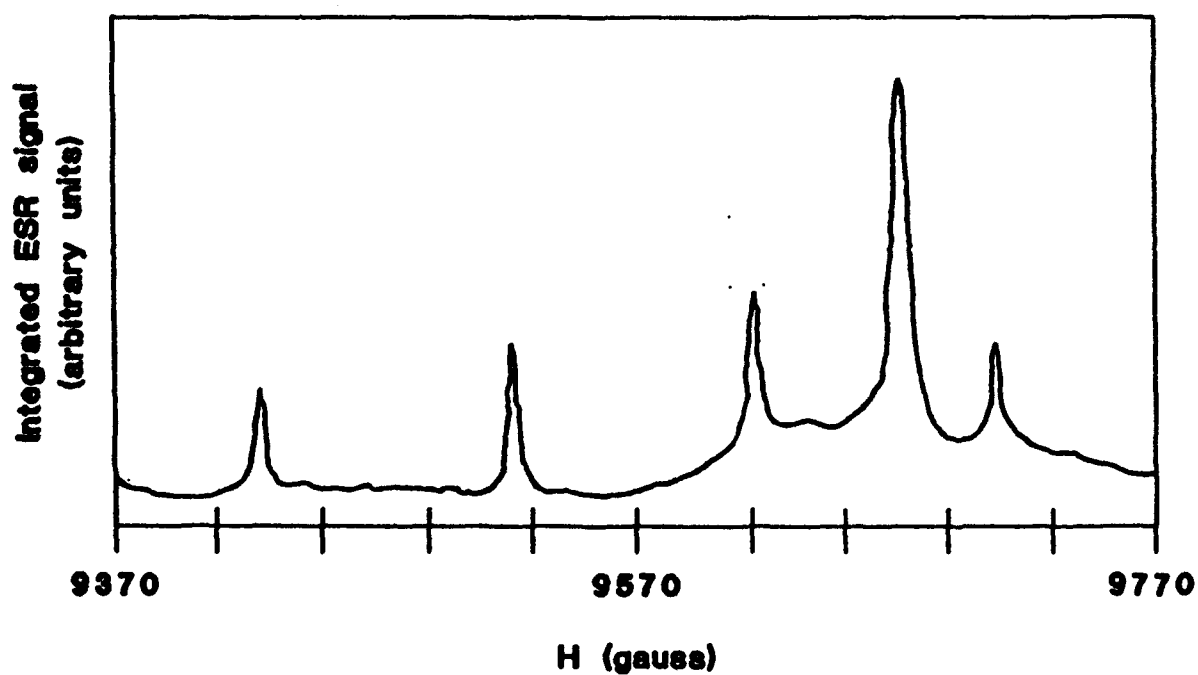
b) First integral of observed signal showing absorption feature.

Figure 19. Complete ESR spectrum of $O_2(a)$ $J = 2$ at $\nu = 8.92$ GHz.

transition. The $O_2(a^1\Delta)$ M_J = -1 → 0 and -2 → -1 transitions should be avoided in these calibration procedures due to convolution effects with this strong ground state feature (Fig. 19). Thus, the stronger of the remaining lines, the M_J = 0 → 1 transition at H = 9522 G, was typically used to monitor $O_2(a^1\Delta)$ concentrations. A high resolution scan of the $O_2(a^1\Delta)$ J = 2 M_J = 0→ 1 transition centered at H = 9522 G is shown in Figure 20 and the $O_2(X^3\Sigma)$ K = 3 J = 4 M_J = 3 → 4 transition at H = 9188 G is shown in Figure 6. A strong signal with moderate modulation is achieved and a nearly complete integration of the signal over the 20 G scan width is obtained.

The transitions shown in Figure 19 are pressure and modulation broadened. Characterization of the line shape profiles including broadening coefficients, Voight fits, and spectral area integrations is described in the following paragraphs.

Pressure broadening has a significant effect on the line shapes observed during the calibration procedure. The pressure broadening of the $O_2(X^3\Sigma)$ by collisions with oxygen has been previously reported as 1.40 (Ref. 43) to 1.87 G/Torr.[*] The pressure broadening observed in the present apparatus is shown in Figure 21 and provides a broadening coefficient of 1.70 ± 0.16 G/Torr. The observed line shapes are also modulation broadened. It has been previously established both experimentally and theoretically that the area, or second integral, of an EPR spectrum increases linearly with modulation amplitude (Ref. 43). As seen in Figure 22a this linear relationship is verified under the operating conditions of this work. The peak-to-peak width of the EPR signal also increases with modulation amplitude (Fig. 22b).

Modulation broadening has been examined in detail (Refs. 28-32). Modulation broadening generally affects the central portion of the EPR spectrum and the wings are relatively unaffected (Ref. 23). For a Lorentzian profile with modulation broadening, the maximum EPR signal occurs when the modulation

---

[*] Ibid, page 17.
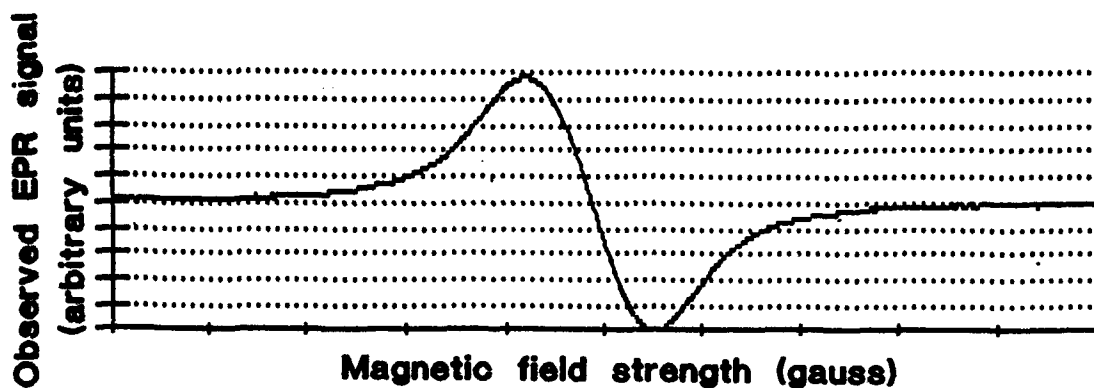
a) Observed ESR signal.
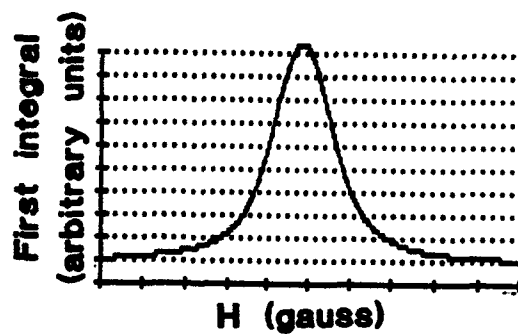
b) First integral of ESR signal (absorption profile).
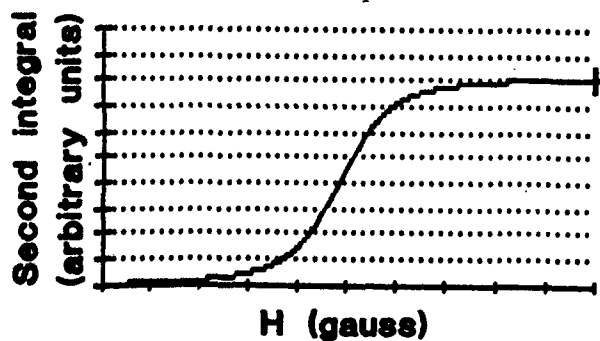
c) Second integral of observed signal used for obtaining areas.

Figure 20. High resolution ESR spectrum of $O_2(a)$ $J = 2$, $M_J = 0 \rightarrow 1$ transition at $\nu = 8.92$ GHz.
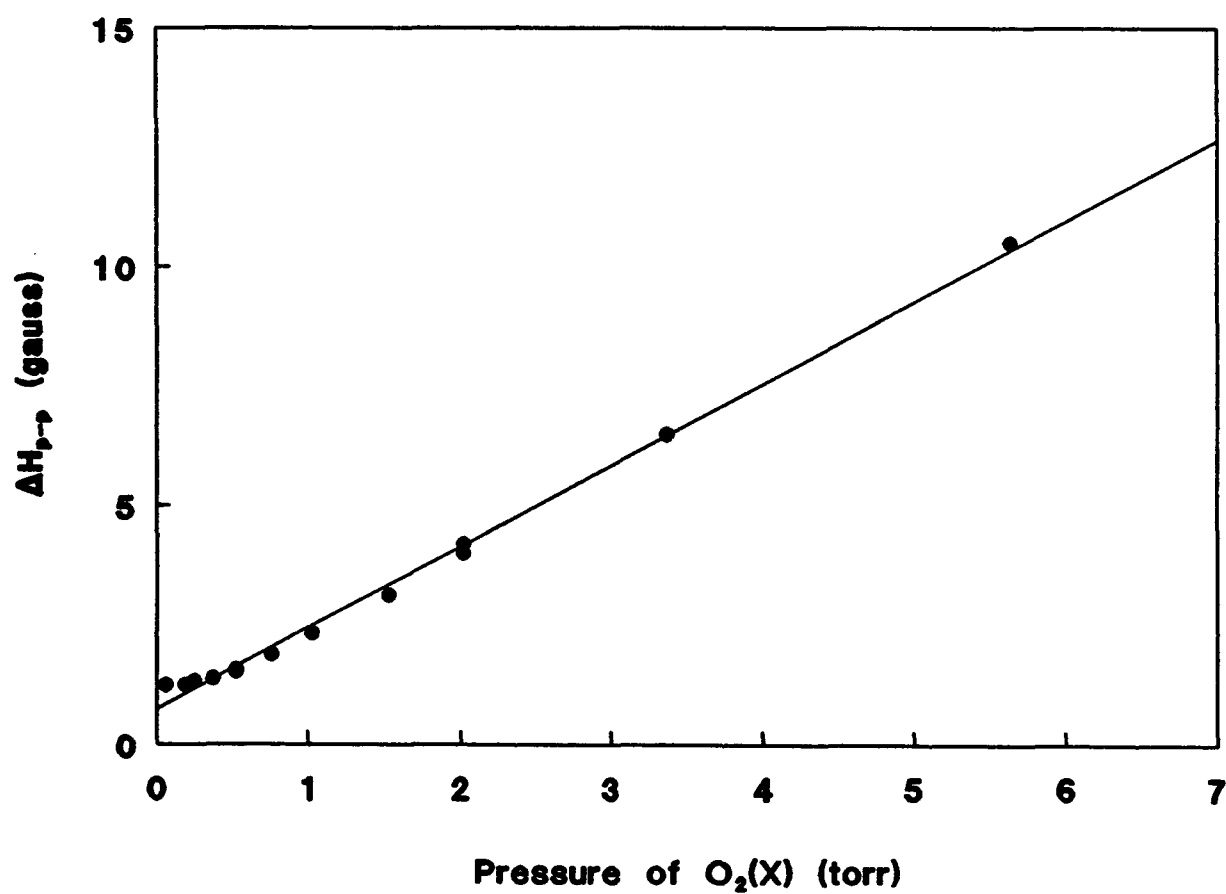
Figure 21. Pressure dependence of observed $O_2(X)$ ESR line shape.
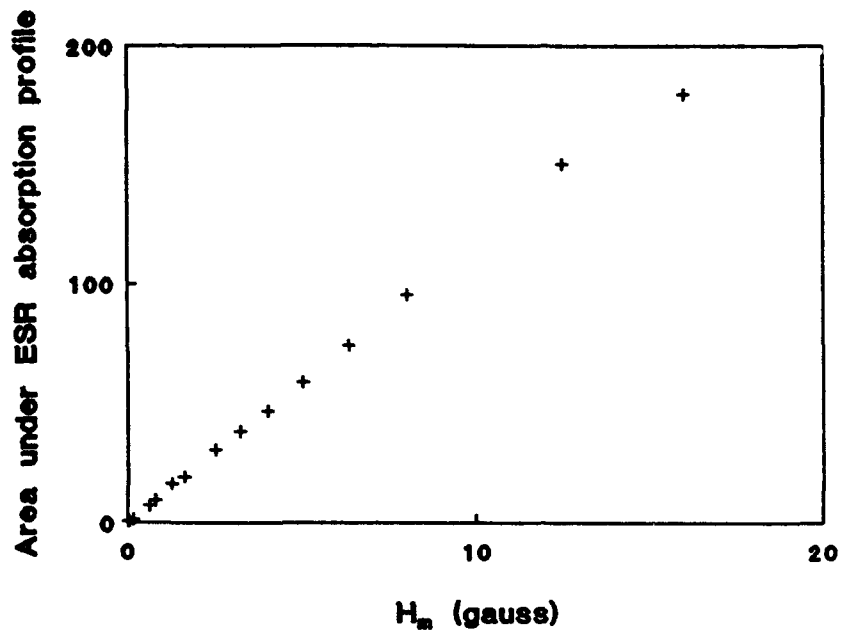
a) Integrated ESR signal as a function of modulation amplitude.
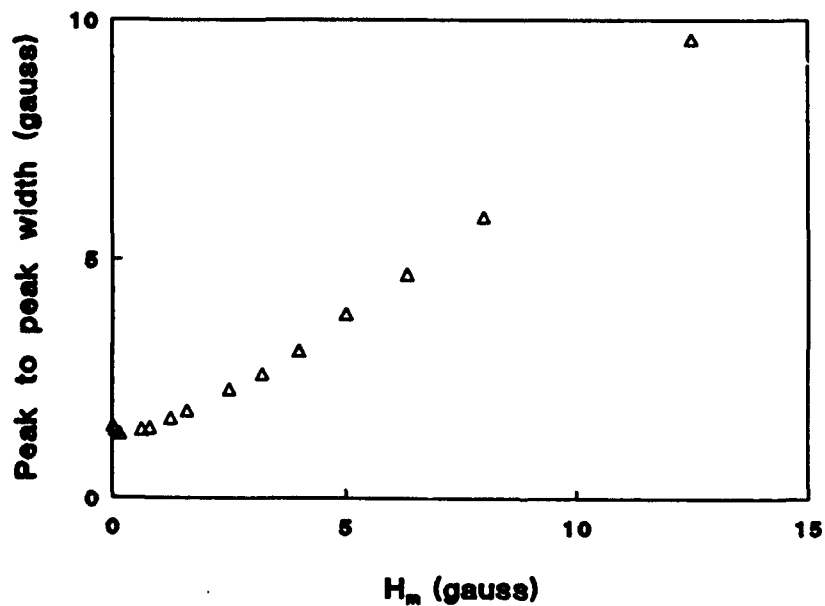
b) Peak-to-peak width of the ESR signal as a function of modulation amplitude.

Figure 22. Modulation broadening of $O_2(X)$ ESR signal.

amplitude is ≈ 1.5 times the peak-to-peak width (Ref. 23). Modulations this great could not be reached with the apparatus used in this work, but the observed areas increase to modulations as high as 75 percent of the peak-to-peak width. Figure 23 shows the observed line shapes are strongly affected for modulations > 50 percent of the line width. Typically, a modulation intensity of H = 0.8 G was used to avoid these strong modulation effects.

The observed line shapes were fit to Lorentzian, Gaussian, and Voight profiles using a Gauss-Newton routine. Figure 24 shows the comparison of these fits with the observed data. The observed line shape is intermediate between Gaussian and Lorentzian and is reasonably well fit by the convolved Voight profile. The Voight profile for $O_2(X^3\Sigma)$ underestimates the signal far from resonance by as much as 20 percent, but reproduces the integrated area to within 5 percent.

Similar results are achieved for $O_2(a^1\Delta)$ with the Voight fit shown in Figure 24b. For an $O_2(X^3\Sigma)$ at a total pressure of 0.48 torr, at the EPR the ratio of Gaussian width to Lorentzian width, $\eta = \Delta\nu_d/(\Delta\nu_L\sqrt{ln2})$, is $\eta = 3.8$, indicating the Lorentzian contribution to the line width is ≈ 27 percent of the resultant width and the Gaussian contribution is ≈ 86 percent (Ref. 27).

The relative intensities of the $O_2(a)$ and $O_2(X)$ EPR transitions were required for the calibration (Eq. 8). An observed EPR spectrum was proportional to the derivative of the absorption profile, thus a double integration of the spectra led to the relative intensities. The integration was limited to a finite magnetic field scan due to interferences from other spectral features. In the present study scan widths of 20 or 40 G were typically used and constituted 5 to 10 times the width of the spectral feature. Figure 25 illustrates the error associated with truncating the integration for both Gaussian and Lorentzian line shapes. The scan widths of the present study introduces essentially no error for Gaussian profiles, but as much as 30 percent error for Lorentzian profiles (Ref. 23).

Since the observed profiles are only approximately fit by a Voight line shape, an experimental test of the truncation error was required. A Voight fit to a

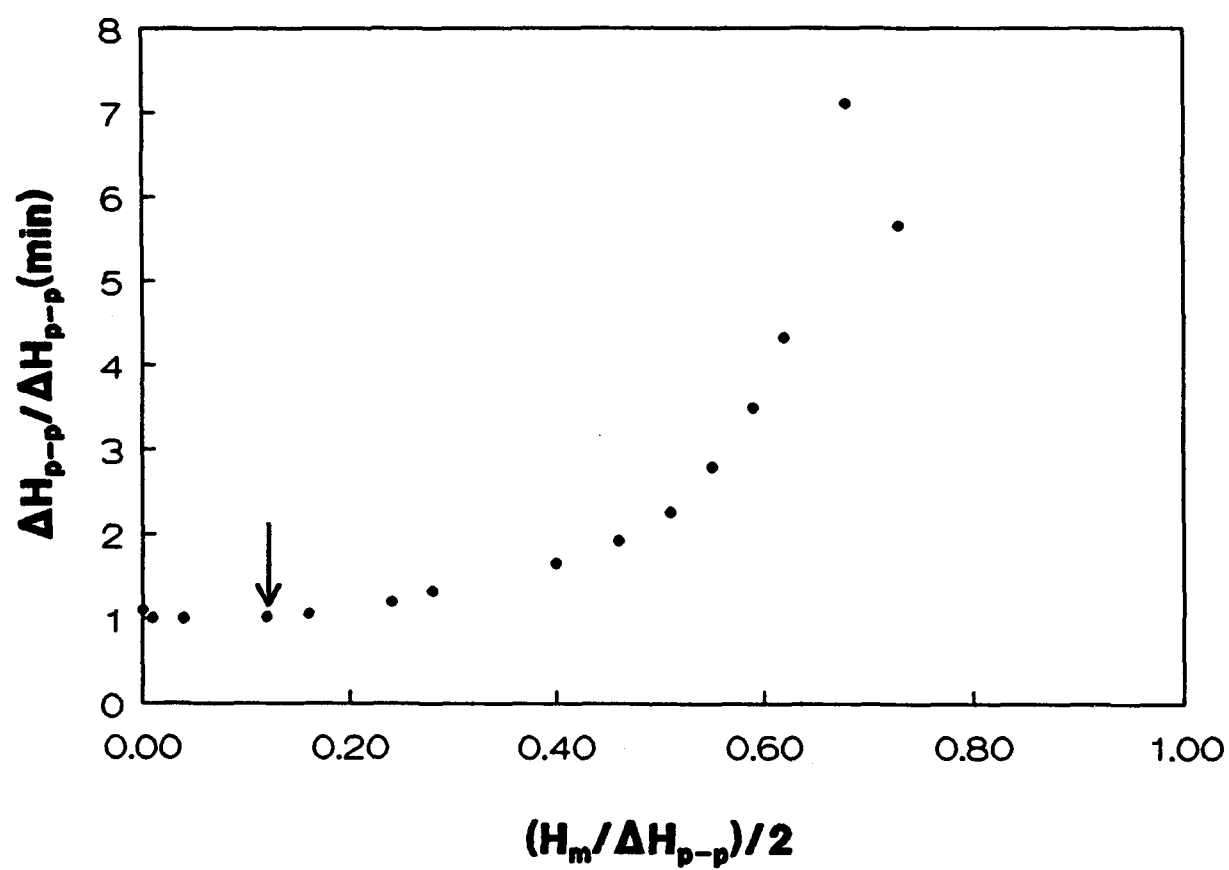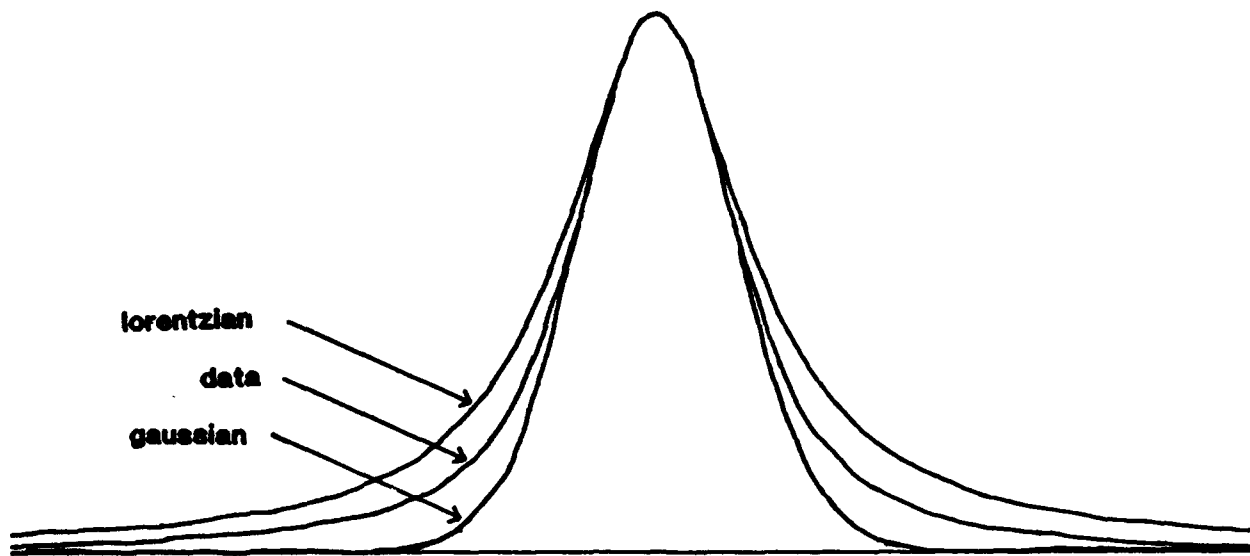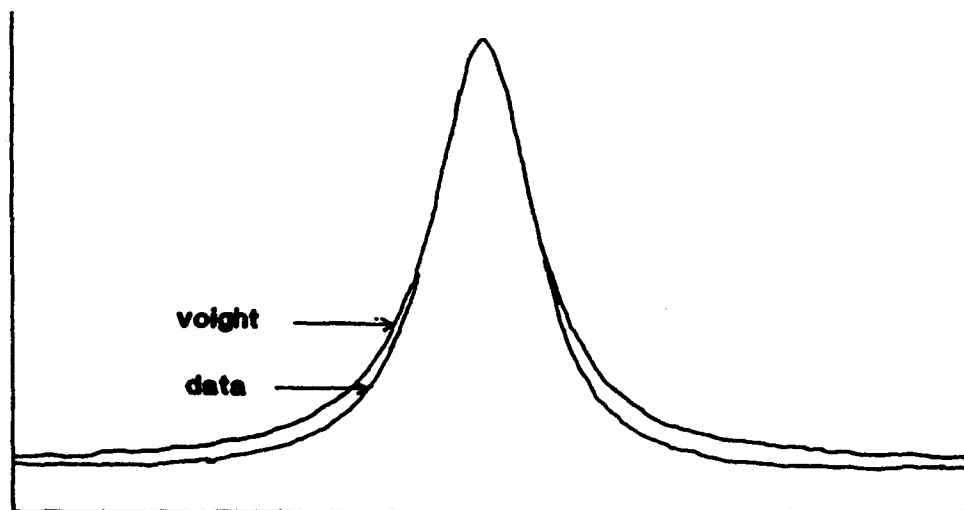Figure 23. Normalized ESR profile width as a function of magnetic field modulation amplitude.

a)   Lorentzian and gaussian fits to the integrated ESR profile.

b)   Voight fit to integrated ESR profile.

Figure 24.   Comparison of integrated ESR profiles with standard line shapes.
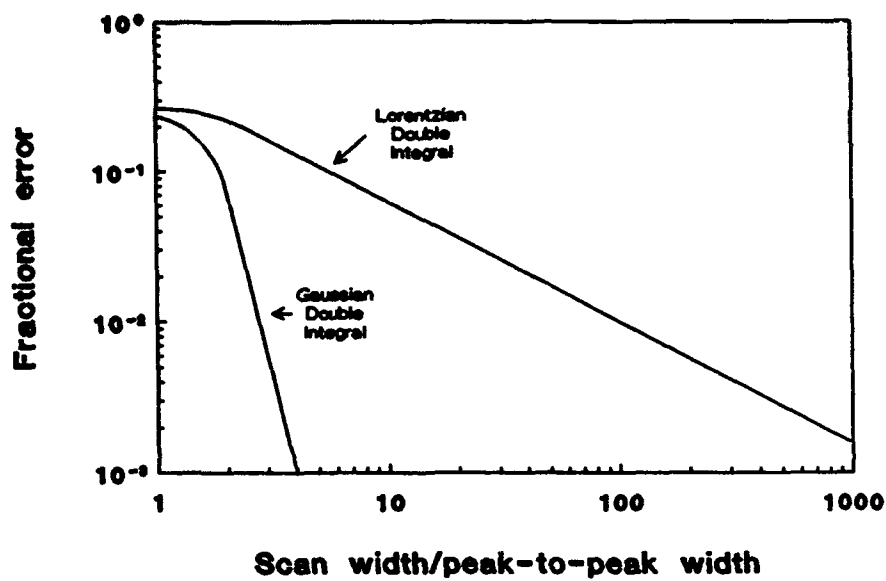
Figure 25. Integral truncation errors.
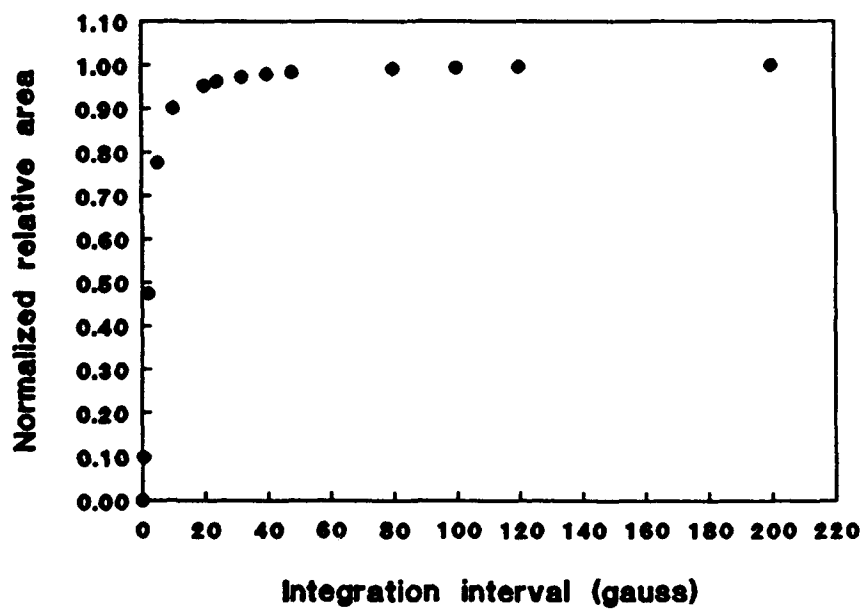
Figure 26. Area under absorption profile as a function of
magnetic field scan width.

20 G scan of the $O_2(X)$ line used the calibration was made. Using these fit parameters, the Voight profile was extended to a width of up to 200 G. Figure 26 presents the dependence of the calculated integrated area for various field scan widths of these Voight profiles. The integrated area versus scan width is relatively flat, but does increase by about 6 percent from a 20 G scan to a 200 G scan. This error is intermediate between the Lorentzian and Gaussian errors shown in Figure 25. The double integral of the observed absorption feature also supports this near complete integration. Figure 20c shows the spectral area as a function of field strength and is nearly flat for field widths above 25 to 30 G.

No theoretical correction for the integral truncation error was made in the present study. A Lorentzian wing correction was not justified since the line shape had considerable Gaussian nature. The truncation error was small for a given spectrum and was further reduced since only the ratio of two observed areas was required for the detector calibration. A quantitative evaluation of the truncation error is provided in Section 5.0.

An inhomogeneous magnetic field may lead to asymmetric ESR absorption spectra. The symmetry of an ESR profile may be determined from the first integral of the original ESR profile. A symmetric absorption profile has even symmetry about the profile peak. The symmetry of the first integral profile was checked by comparing pairs of points equidistant in field from the peak. In the present experiment the maximum difference between a pair of points was 1.2 percent, indicating near symmetry. This symmetry justified averaging the points in an observed ESR spectrum to calculate the baseline (Ref. 23).

The effects of microwave power saturation were examined in the present study and the results are presented in Figure 27. If the rate of stimulating transitions between spin states approaches the rate of spin state relaxation, the transition becomes power saturated (Ref. 23). Saturation has been observed on the $O_2(X^3\Sigma)$ K = 3, J = 4, M_J = 3 → 4 transition at microwave powers of about 40 mW (Ref. 6). A linear fit to the low power, <100 mW, portion of the curve provides a near-zero intercept and a good correlation of
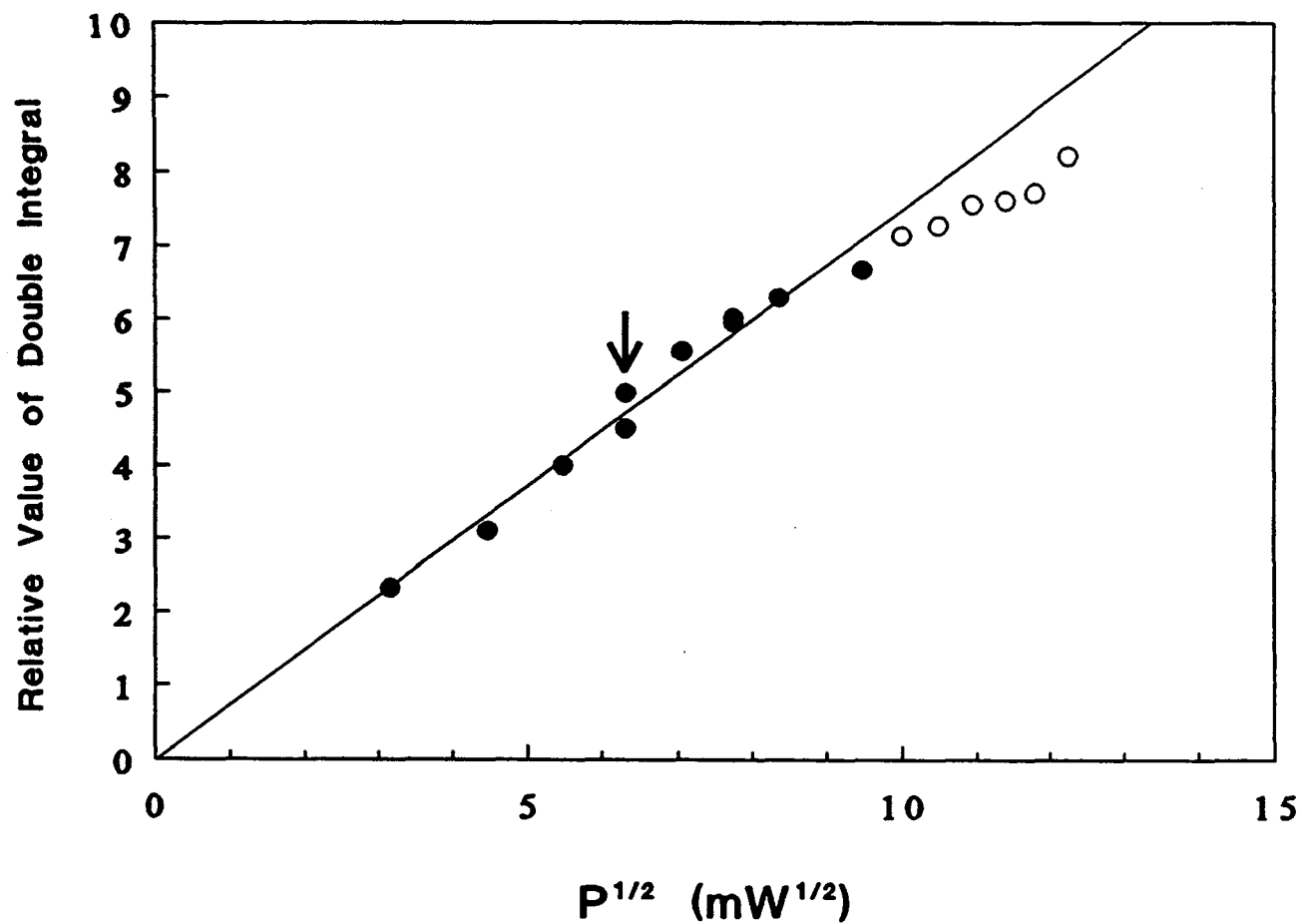
Figure 27. Effect of microwave power on the area under the absorption profile.

r = 0.973. The curve of Figure 27 begins to deviate from this linear response at Klystron powers above 100 mW. To avoid the possible complications of saturation effects, microwave powers of 40 mW were used in the present studies.

The relative EPR gain settings, G_i, are critical to the absolute $O_2(a^1\Delta)$ concentration calibrations, as seen in Equation 10. The relative peak intensities are plotted as a function of the gain up to 8000 in Figure 28. The y-intercept is zero within error, -0.15 ± 0.19, and the correlation to a linear fit is 0.99987. The instrumental gain settings were accurate.

The linearity of the EPR apparatus was verified by observing the integrated areas of the $O_2(X)$ EPR absorption features for various flow rates of pure $O_2(X)$. Figure 29 demonstrates a linear EPR response with a correlation of r = 0.9933 and a standard deviation of σ = 30.8. The intercept is zero within the uncertainty of the data. The scatter in the data of Figure 29 is primarily due to the reproducibility of observed EPR integrated absorption areas.

Typically, the ratio of areas from $O_2(^1\Delta)$ and $O_2(X^3\Sigma)$ spectra were calculated to determine the fraction of $O_2(^1\Delta)$ to total oxygen concentration. This assumed that with the microwave discharge on, the oxygen flow consisted of only these two species. Another method for calculating the ratio of $O_2(^1\Delta)$ to total oxygen which makes this assumption is to compare the EPR signals of $O_2(X^3\Sigma)$ with the microwave discharge on with the microwave off.

$$[O_2(a^1\Delta)] = [O_2(X^3\Sigma)]_o - [O_2(X^3\Sigma)] \tag{28}$$

where:

$[O_2(X^3\Sigma)]_o$ = ground state concentration when microwave is off

$[O_2(X^3\Sigma)]$ = ground state concentration when microwave is on

This difference method is not preferred since small changes in large signals are obtained. Figure 30 illustrates the ratio $[O_2(^1\Delta)]/[O_2(X^3\Sigma)]$, calculated by the difference method (Δ) and the observed $O_2(a)$ EPR signals (+). The two
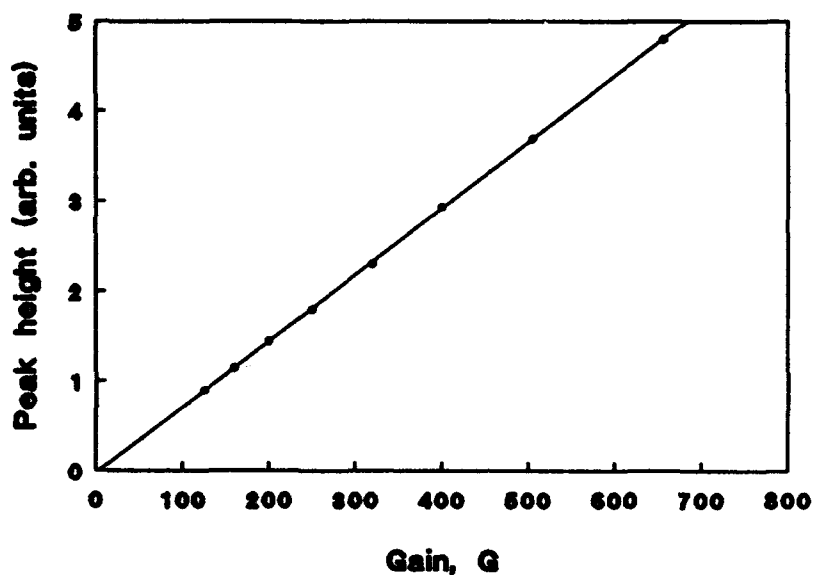
a) Low gain
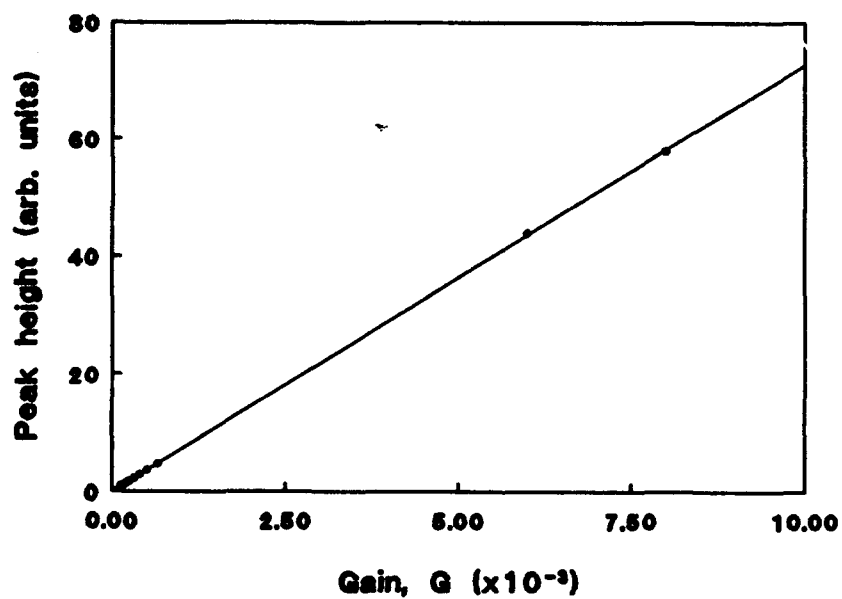
b) High gain

Figure 28. Peak heights of $O_2(X)$ ESR profiles for various gain settings.
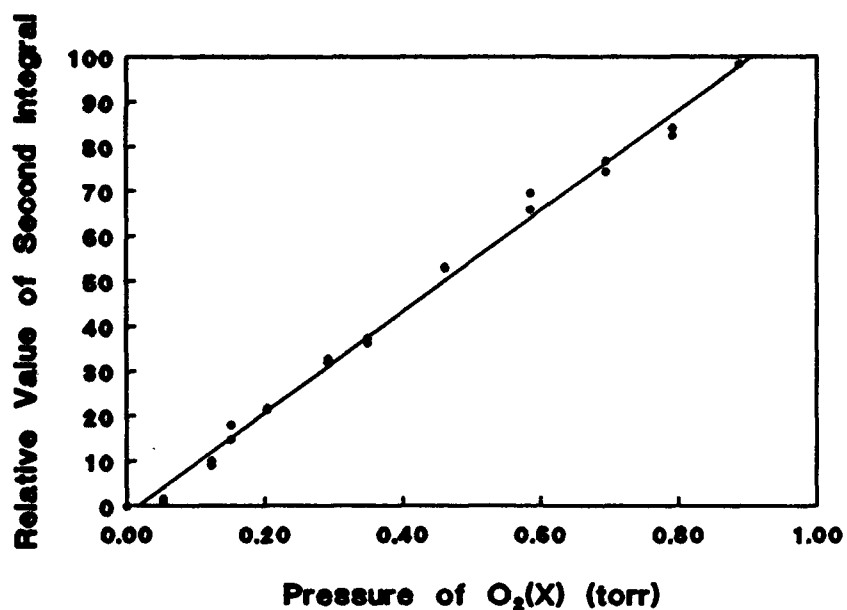
Figure 29. Area under absorption profile as a function of $O_2(X)$ pressure.
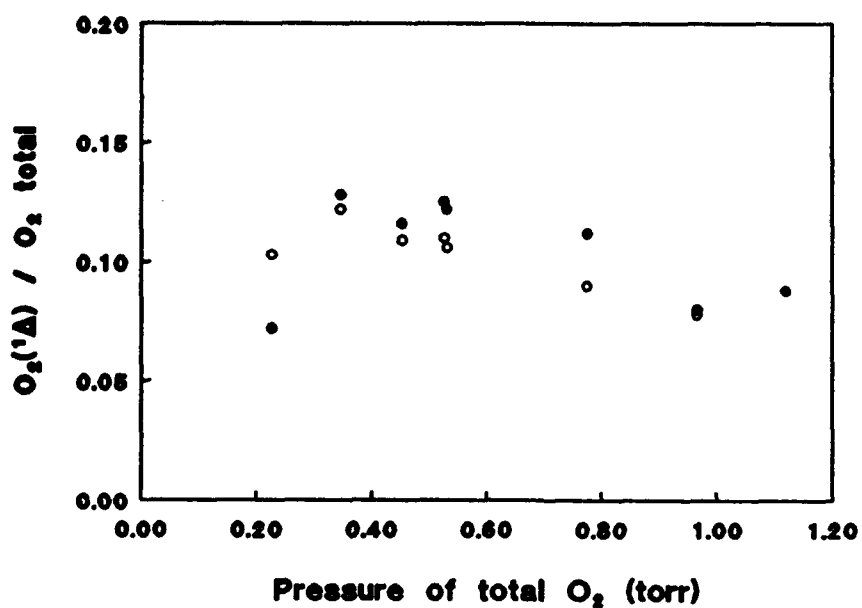
Figure 30. Comparison between difference and ratio methods for determining the fraction of $O_2(a)$.

methods agree to within 2 percent. This approach provided a quick system check and indicated that the microwave discharge produced no high concentrations of other excited states of oxygen.

The difference in these two results could be attributed to the presence of $O_2(b^1\Sigma)$. An estimate for the concentration of $O_2(b)$ can be made from the kinetic analysis presented in Section 2.4. The steady-state concentration of $O_2(b)$ is

$$[O_2(^1\Sigma)] = k_{13}[O_2(^1\Delta)]^2/(k_{20} + k_{18}[O_2(^3\Sigma)]) \tag{29}$$

For a wall rate of $k_{20} = 20$ s^{-1} which corresponds to a deactivation probability of $\gamma = 10^{-2}$ in a 2.54-cm diam tube at a velocity of 10^3 cm s^{-1}, the singlet sigma concentration is $\cong 10^{12}$ molecules per cubic centimeter, or 0.1 percent of the the $O_2(^1\Delta)$ concentration. This calculation is sensitive to the wall rate and if a slower rate is chosen so that the deactivation is controlled by gas phase quenching, then an upper bound to the $O_2(b)$ concentration of ~ 5 percent of $[O_2(a^1\Delta)]$ is obtained. Thus, the differences observ_ in Figure 30 could be partially attributed to $O_2(b)$ or may simply reflect systematic differences in the measurements.

4.0 RESULTS AND CALIBRATION DATA

The infrared detection system calibration is determined by plotting the concentration of $O_2(a^1\Delta)$ versus the observed detector voltage, V_{IR}.

$$[O_2(a^1\Delta)] = CAL\ V_{IR} \tag{30}$$

The detector voltage is measured directly at the diagnostic duct. The $O_2(a^1\Delta)$ concentration is calculated from the observed EPR spectra and corrected for transport losses to provide the concentration at the diagnostic duct. The analysis of Section 2.4 is used below to derive the quantity $[O_2(a^1\Delta)]$ at the diagnostic duct.

Equation 31 provides the relationship between observed EPR spectra and concentration of $O_2(a^1\Delta)$ at the EPR cavity:

$$[O_2(a^1\Delta)]_{EPR} = [r/(1 + r)]\ (P_{EPR}/K_B T) \tag{31}$$

where:

$$r = (I_{O_2(a)}/I_{O_2(X)})\ (G_{O_2(a)}/G_{O_2(X)})\ (0.624) \tag{32}$$

The pressure at the EPR cavity, P_{EPR}, is calculated from the friction loss Equation 33 and the observed pressures at detection blocks B1 and B2. The distances are measured from the EPR.

$$P_{EPR}^2 = P_1^2 + (P_2^2 - P_1^2)\ (x_{EPR} - x_1)\ /\ (x_2 - x_1) \tag{33}$$

where:

x_2 = position of detection block B2 = 41.9 cm

x_1 = position of detection block B1 = 54.6 cm

x_{EPR} = position of EPR cavity = 0 cm

P_1 = pressure at block B1

P_2 = pressure at block B2

57

The gas temperature in Equation 8 was measured at blocks B3, B2, and at the duct and was independent of position, x. The temperature at the calibration duct was measured 8.9 cm from the optical windows.

The data from a typical calibration conducted on 19 February 1987 are provided in Table 4. For the locations of various measurements, refer to Figure 10. Reducing the data according to the above procedure provides the calibration plot shown in Figure 31. The plot had a linear correlation of r = 0.9980, a near zero intercept of 0.002 ± 0.01 and a slope calibration factor, CAL = 1.60 x 10^{15} ± 0.01 cm^{-3}.

Table 4. Sample calibration data

Run No.	Pressure (torr)				Signal (volts)				Flow rate (sccm)			
	B1	B2	B3	Duct	B1	B2	B3 (Cable)	A	Duct B	C		
1	0.402	0.526	0.575	0.554	0.55	0.72	1.3	1.0	1.4	1.22	201
2	0.264	0.346	0.380	0.365	0.33	0.46	0.91	0.75	1.07	0.95	201
3	0.163	0.214	0.236	0.226	0.23	0.32	0.75	0.46	0.65	0.57	52
4	0.098	0.127	0.141	0.135	0.11	0.16	0.52	0.24	0.34	0.32	30
5	0.345	0.453	0.495	0.477	0.44	0.62	1.13	0.85	1.16	1.04	149
6	0.405	0.531	0.582	0.560	0.52	0.70	1.25	0.95	1.29	1.18	200
7	0.511	0.669	0.731	0.705	0.60	0.82	1.43	1.17	1.60	1.38	300
8	0.593	0.775	0.847	0.817	0.67	0.90	1.53	1.24	1.73	1.52	402
9	0.742	0.966	1.055	1.02	0.73	1.0	1.67	1.36	1.92	1.65	602
10	0.862	1.12	1.22	1.18	0.79	1.08	1.75	1.46	2.08	1.80	800

This calibration does not account for $O_2(a^1\Delta)$ deactivation during the transport from the diagnostic duct to the EPR cavity. The analysis of Section 2.4 provides the basis for making the necessary deactivation correction. The transport of $O_2(a^1\Delta)$ is described by Equation 34:

$$[O_2(a^1\Delta)]^{-1} = \{ [O_2(a^1\Delta)]_o^{-1} + A/B \} \exp (Bt) - A/B \qquad (34)$$
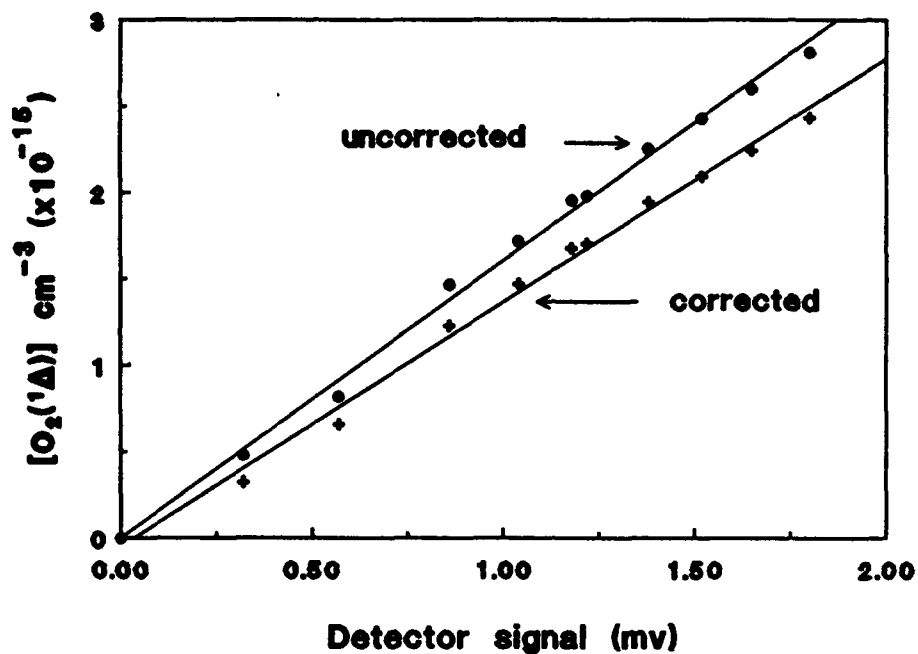
Figure 31.   The $O_2(a)$ detector calibration plot.
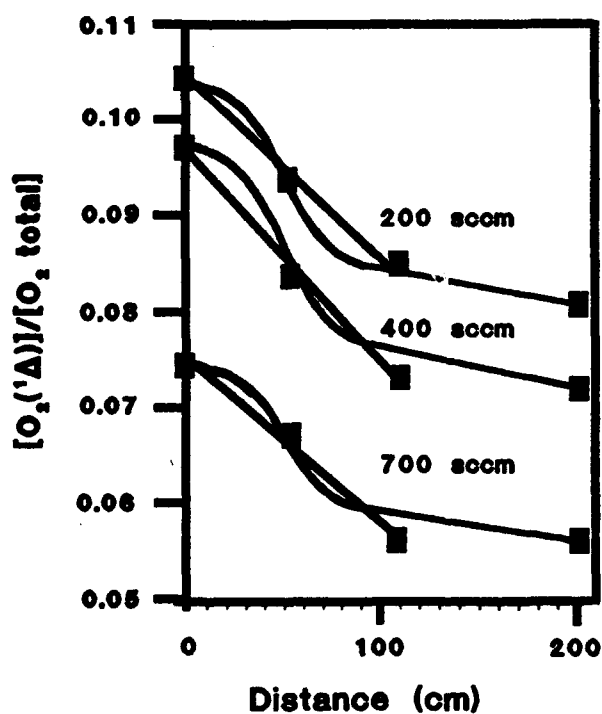
Figure 32. Linear approximation for kinetic deactivation of $O_2(a)$.

The deactivation observed in the present apparatus is small, usually less than 20 percent between block B3 and the EPR, and Equation 34 can be simplified by the approximation $\exp(Bt) \approx 1 + Bt$:

$$[O_2(a^1\Delta)]^{-1} = [O_2(a^1\Delta)]_o^{-1} + \{ [O_2(a^1\Delta)]_o^{-1} + A/B \} Bt \qquad (35)$$

This inverse linear relationship provides for a simple deactivation correction. In Figure 32, the concentration of $O_2(a)$ is shown as a function of flow distance.

The IR detector signals at blocks B1, B2, and B3 directly provide a relative measure of the $O_2(a^1\Delta)$ concentration and were used to assess the value of the term:

$$\{ [O(a^1\Delta)]^{-1} + A/B \} Bt \qquad (36)$$

That is, the slope is determined by the measured IR detector signals and a linear interpolation is used to correct for deactivation between the diagnostic duct and the EPR cavity. Note that the observed IR detector signal depends on both the fraction of $O_2(a^1\Delta)$ in the flow and the total pressure. The pressure drops between detection blocks due to friction losses and must be accounted for by the relationship:

$$V_{IR} \propto P \left([O_2(a^1\Delta)] / [N_T] \right) \qquad (37)$$

Thus, the correct dependent variable for Figure 31 is:

$$[O_2(a^1\Delta)]^{-1} \propto P / V_{IR} \qquad (38)$$

Since the diagnostic duct and entrance ramps are spatially symmetric and the optical viewing port is at the midpoint, one-half of the observed deactivation between blocks B3 and B2 is attributed to the deactivation between the diagnostic duct and block B2. Almost no deactivation occurs between blocks B2 and B1 due to high flow velocity in this narrow channel.

The calibration plot corrected for deactivation by the above procedure is given in Figure 31. Again, the plot is quite linear with a correlation of r = 0.9972, has a near zero intercept, -0.05 ± 0.01, and accurately defines the calibration factor, CAL = 1.41 ± 0.01 x 10^{15} cm^{-3}. The transport deacti-vation correction reduces the calibration by $\cong$ 5 percent.

The calibration must provide a linear plot with zero intercept. Otherwise, significant systematic errors are indicated. In particular, a nonzero inter-cept may result from significant atmospheric leaks and a high background pressure.

A more sophisticated study of the kinetic deactivation due to transport was conducted using the DEACT computer model (Ref. 42). A complete description of the gas phase kinetics of oxygen (Ref. 33) was coupled with a two-dimensional fluid dynamics code to predict $O_2(a^1\Delta)$ concentrations as a function of flow distance for the calibration apparatus geometry. A comparison of the observed data and model predictions is shown in Figure 32. Deactivation is greatest in the diagnostic duct where the flow velocity is lowest. Also shown in Figure 32 is a linear interpolation between blocks B3 and B2. While the deactivation is not linear between these blocks, it is symmetric and the linear and exact calculations agree at the midpoint.

The data of Figure 32 were not well fit by a single deactivation rate. The modeled results were obtained with a single parameter, the wall deactivation rate, defined as a probability, γ. To successfully reproduce the data, the parameter γ was allowed to vary as a function of flow rate. While this approach is not physical, it does allow for good agreement with the data. A more precise and detailed study to characterize the deactivation of singlet oxygen on surfaces is underway (Ref. 44).

5.0 ERROR ANALYSIS

The purpose of this section is to address all known sources of error associated with the calibration. No rigorous statistical analysis is presented; however, the estimated error in measured quantities is given. Considerable thought has gone into addressing all possible sources of systematic errors. The most important conclusion of this section is that the single largest source of error in the calibration is the uncertainty associated with the singlet delta EPR signal. Refer to List Of Symbols for definitions of the variables shown in the tables.

5.1 STATISTICAL ERRORS OF MEASURED AND DERIVED QUANTITIES

The random (or statistical) error in each measurable quantity has been estimated, based on experience gained from performing hundreds of EPR scans. These estimated errors are summarized in Table 5. Since the measured values nearly always fell within these error limits, these errors can be considered estimates of the 95 percent confidence limit.

Table 5. Resolution and statistical error in observed quantities.

Measurable Quantity	Instrument Resolution	Typical Value	Estimated 95 Percent Confidence Limit
T	0.1 K	294 K	0.3%
P	0.2 %	0.1 - 1.5 Torr	0.5%
$\dot{m}$	1.0 %	50 - 2000 sccm	0.5%
Δx	1 mm	1000 mm	0.1%
r_o	0.1 mm	10 mm	1.0%
V_{IR}	0.01 mV	0.3 - 2.0 mV	1.0%

The errors in derived quantities such as velocity, $[O_2(a^1\Delta)]$, and the calibration factor, Cal, are obtained by the appropriate propagation of errors (Ref. 45) and are reported in Table 6. Briefly, the error in a derived quantity is the total derivative of that quantity divided by the value of the quantity, dq/q, where the total derivative is obtained by partial differentiation with respect to all the independent variables. In some cases the analytic expression for the partial derivative has been approximated to provide a constant, numerical coefficient to the error in measured quantities. The derived errors are provided in Table 6.

By far the greatest source of statistical error is provided by the observed EPR spectrum, $\alpha'(H)$, for $O_2(a)$. Indeed, the 12 percent variations in observed EPR absorption signals, due to the poor signal-to-noise ratios at these low $O_2(a)$ concentrations, directly translates into a 20 percent error in the resultant calibration. None of the observed errors are limited by instrument resolution or the precision of required constants.

Table 6. Statistical errors of derived quantities.

Quantity	Calculated Error
pressure in EPR cavity (P_{EPR})	0.9%
gas velocity (v)	3.8%
Integral of Absorption $(I_{O_2 x})$	1.0%
Integral of Absorption $(I_{O_2 a})$	12.0%
Fraction of singlet delta by ratio method	13.0%
Fraction of singlet delta by difference method	18.0%
Partial pressure of Singlet Delta $(P_{O_2(a)})$	14.0%

5.2 SOURCES OF SYSTEMATIC ERRORS

The potential sources of systematic error are identified in Table 7. Extreme
care was taken to check for systematic errors and eliminate them. Following
the table is a discussion of each source of systematic error.

Table 7. Primary sources/symptoms of systematic errors.

nonzero Cal plot intercept
nonlinear Cal plot
nonzero pump curve intercept
Assumption that only $O_2(X,a)$ present
integral truncation
spectral interference
nonsteady flow
deactivation correction
improper H amplitude calibration
EPR signal $(\alpha'_{O_2X}(H))$
EPR signal $(\alpha'_{O_2a}(H))$
EPR Gain Setting (G)
Magnetic Field Scan (ΔH_{scan})
Modulation (H_m)
EPR Microwave Power (P_μ)

A nonzero intercept in a calibration plot is a strong indication of serious
systematic errors. Experimental problems such as: (1) the detection of
background light or extraneous emissions, (2) substantial vacuum leaks, (3)
significant kinetic deactivation, (4) nonlinear response of detection systems

(IR sensor or EPR spectrometer), or (5) equipment malfunction can lead to such non-zero intercepts. As shown in Figure 31, the intercepts observed in the present study are zero, within experimental error. This should be the case for any reliable calibration. Similarly the calibration plot should exhibit no curvature. The linear correlation coefficient for the calibration plot corrected for deactivation is r = 0.9979, and thus no significant systematic errors were apparent.

A large leak rate or zero offset in mass flow controller or pressure trans-ducer can lead to a nonzero intercept in Figure 18. While the calibration factor does not depend on mass flow rate directly, the deactivation correction does depend on velocity which is obtained from flow rates. This constant offset effect will cause the greatest percentage error at very low flow rates and longest deactivation times. Since the deactivation correction is always less than 12 percent in the present apparatus and an offset of 5 percent of the total flow will cause a small error in velocity, and a negligible error in the calibration.

The presence of species other than $O_2(X)$ and $O_2(a)$ in the flow from the microwave source is rather limited. Typically the concentration of $O_2(b^1\Sigma)$ is about 1 percent of the total O_2 flow and oxygen atoms account for only about 1 in 10^6 particles. These results agree with the predictions of the difference method for determining the concentration of $O_2(a)$ provided by Equation 8. The error in integrated area introduced by the finite field scan width of 20 G was established in Section 3.0 as < 6 percent.

The truncation error always underestimates the area of the spectral feature. Since only the ratio of $O_2(a)$ concentration with respect to $O_2(X)$ is needed, it is the difference in truncation errors for the two scans that introduces any systematic error. It is more difficult to experimentally determine the truncation error for $O_2(a)$ due to the greater extent of noise in the spectrum. Thus the relative truncation error can only be estimated. The truncation error is primarily dependent on the ratio of spectral feature width (ΔH_{pp}) to the scan width (ΔH_{scan}). The absorption profile widths of $O_2(a)$ and $O_2(X)$

were s the same within experimental error. Therefore, the relative truncation error is negligible.

No emission signals were observed at the IR detector above the dark signal of 0.01 mV. Neither background radiation from the room nor NO + O recombination emission were detectable in the present apparatus and introduced no error in the calibration.

The microwave source of $O_2(a)$ must be extremely stable to prevent any changes in flow conditions or partial pressures during the time required to obtain all EPR spectra. The characterization of the present apparatus established no long term drift in the $O_2(a)$ source and local fluctuations of <0.5 percent. A chemical source of $O_2(a)$ would not be nearly as stable.

The observed EPR line positions and line widths agree well with those previously reported. However, no direct determination of the magnetic field strength was accomplished in the present study. The present calibration facility should be modified to provide a direct determination of magnetic field strength.

Proper maintenance of the fiber optics bundles is critical. The detector collection efficiency can be severely affected by: (1) changing or re-installing the fiber optic bundle, (2) stressing or bending the fiber bundle, (3) changing the very sensitive focus of the collimating optics by flexing the cable or re-orienting the optic mount, or (4) chipped or dirty fiber end surfaces. The complete detection system including collection optics and fiber optics should be maintained as an integral system.

The infrared detectors must be maintained at liquid nitrogen temperatures to insure maximum sensitivity since the detector response is temperature-sensitive. Also, the voltage supplied to the detector must remain at - 250 V DC for proper operation.

In applying the diagnostic to COIL devices, one must be careful to ensure that the windows or diagnostic ports on the device are not affected by device oper- tions. Often, the windows can be coated with salts or other flow contaminates that may severely degrade the detector collection efficiency.

Periodic checks, possibly through relative blackbody calibrations, are criti- cal to assessing any changes in the performance of the diagnostic during a series of laser test sequences.

5.3 TOTAL ERRORS ASSOCIATED WITH CALIBRATION

In light of the previous discussions, the following error estimates are recommended.

> statistical error: 20 percent
> systematic error: negligible
> total error: 20 percent

These quoted errors are for the calibration factor, Cal. To obtain the error associated with measured $O_2(a)$ concentrations, the statistical uncertainty in the measured detector voltage when viewing the COIL gas medium must be included. Typically, this additional source of error is small. The quoted error does not apply to the yield of singlet oxygen, as the uncertainty in any ground state oxygen measurement may be large and has not been included. Finally, yields are often quoted in percentages and the above relative errors in $[O_2(a)]$ should not be confused with the absolute error in percentage yields.

6.0 DISCUSSION

The method of calibrating $O_2(a^1\Delta)$ emission detectors by EPR spectroscopy has been used by many research groups since 1978 to support the development of Chemical Oxygen-Iodine Lasers (Refs. 4,10-12). Typically, these studies achieved statistical errors of 10 to 15 percent. Probably the best characterized study of systematic errors prior to the current effort is documented in Reference 10. Several discrepancies, recommendations for reducing systematic errors, and problems with transfer calibrations are reported in the previous work (Refs. 10-12). Only a limited number of calibrations were performed on the same, unaltered detection system and thus, little information was available on the long term stability and statistical fluctuations in the calibration factor.

This study provides a detailed examination of the characteristics of the calibration apparatus including excited oxygen flow system, EPR spectrometer, infrared detector system, and data acquisition system. The total calibration error is largely controlled by noise in the observed EPR spectrum of $O_2(a^1\Delta)$ and the statistical error bound is in agreement with previous estimates. However, several improvements in controlling systematic errors are currently reported, including: (1) design of an optical collection and detection system as a single unit to limit the sensitivity of the calibration to geometrical and hardware changes, (2) complete characterization of the excited oxygen flow (fluid dynamics, kinetic deactivation, stability, etc), and (3) enhanced analysis of observed EPR spectra.

Improvements in the apparatus and data analysis have reduced or characterized several important sources of systematic error. Several advantages are obtained by using a single infrared detector to simultaneously sample the signals from three viewing volumes: reduced system complexity and cost, reduced variability between detectors, and direct measurement of relative signals needed for an accurate measurement of kinetic deactivation.

The calibration apparatus has been designed for complete characterization of the excited oxygen flow including a direct measurement of kinetic deactivation between the diagnostic duct and EPR cavity. The construction of the collection optics and the infrared detector as a single unit is absolutely vital in preventing changes in detection efficiency due to hardware configuration. An analysis of the EPR signals including symmetry, baseline, truncation far from resonance, and line shape provides increased confidence in the relative concentration, $r = [O_2(a)]/[O_2(X)]$.

No significant error was introduced from the following sources: NO + O afterglow, IR detector linearity, EPR linearity, transverse pressure gradients, temporal stability of $O_2(a)$ source, inhomogeneous magnetic field (symmetric absorption spectra), and temperature measurements.

Most important is the current assessment of the long term performance of the diagnostic. During a period of 18 months, 5 calibrations were performed on the same detection system and the calibration factors remained constant to within 10 percent. This diagnostic was used extensively on COIL devices. A complete documentation of its performance on the ROTOCOIL device will provided in another document. The consistency of the present methods and apparatus are unparalleled and represent by far the most extensive data base to evaluate the performance of this diagnostic.

Several opportunities exist for increasing the precision of the present diagnostic. In order to decrease the statistical error, a higher concentration of singlet oxygen is required to enhance the observed EPR spectra of $O_2(a)$. This cannot be accomplished with the current microwave source of excited oxygen but might be achieved with a higher power, transverse flow microwave generator similar to those currently being developed to study active nitrogen.[*] While a small chemical generator of $O_2(a)$ could be used, the added complexity and analysis difficulties are considerable.

---

[*] Schlie, L.A., Phillips Laboratory, private communication.

A calibration of the magnetic field strength was not accomplished in the present study and should be undertaken. Any error in the field strength is doubled when propagated through the double integration and accounts for the single largest potential source of systematic error.

An independent determination of wall deactivation rates would assist in the deactivation correction. The observed dependence of wall deactivation probability, γ, on flow conditions is particularly disturbing. The uncertainty in kinetic deactivation is small and only weakly affects the uncertainty in the calibration factor. Thus, the wall deactivation rates are not particularly important to the calibration. Note that the pump curve for this apparatus provides a fixed time between observation points independent of pressure and flow rate.

The NO + O afterglow was not a problem in the current apparatus. A simple diagnostic for potential sources of emission other $O_2(a^1\Delta)$ is readily available and is worth implementing in the experimental apparatus. Specifically, the simultaneous detection of emission at 1.268 μm and 1.315 μm is possible with two narrow band-pass filters and a signal at 1.315 μm would indicate background emission problems.

A semiquantitative assessment of changes in viewing volume was made in the present study. A more complete study, both analytically and experimentally, of the viewing volume, sensitivities to optical focus and hardware geometry, and transfer calibrations to different viewing geometries would be necessary if transfer calibrations were necessary.

The prediction of COIL laser power from the measurement of $O_2(a^1\Delta)$ concentrations has not been completely successful. This may be due to several causes:

· the laser typically operates near threshold conditions and small differences in the yield of $O_2(a^1\Delta)$ produce large changes in output power

• laser power depends more strongly on yield than on $[O_2(a^1\Delta)]$, and a large uncertainty in $[O_2(X)]$ may be present

• a large uncertainty in several important energy loss mechanisms such as iodine dissociation and nozzle mixing efficiency exists

• COIL devices tend to operate more efficiently at higher powers

While a diagnostic for singlet oxygen is absolutely vital to characterizing COIL device performance, its singular predictive capability is limited.

The development of advanced diagnostics for $O_2(X,a,b)$ have been considered by many groups. Two particularly interesting suggestions include absorption on allowed ultraviolet transitions, and microwave absorption techniques. Absorption techniques offer the distinct advantages of simplicity and requires no detailed calibration procedures. However, several problems exist with these approaches. First, accurate determination of the absorption cross section is problematic. Second, pressure broadening effects may limit the resolution of microwave spectra. Absorption due to multiple transitions even at a single wavelength induce difficult deconvolution issues. Possibly more important than improved diagnostics for $O_2(a)$ is the development and implementation of a direct $O_2(X)$ diagnostic.

7.0 CONCLUSIONS

The precise, absolute detection of singlet oxygen is a task requiring great attention to detail and careful experimental methods. Detection by absolute radiometry calibrated by the EPR spectroscopic method is currently the most reliable method for quantifying $O_2(a)$ concentrations for chemical laser applications. A calibration apparatus and detector assembly has been developed, characterized, and documented that provides for reliable imple- mentation on chemical oxygen-iodine lasers. This improved apparatus provides for direct measurement of kinetic deactivation, multiple detections with a single infrared detector, and comprehensive characterization of the calibration equipment. Concentrations of singlet delta oxygen in the range of $7 \times 10^{13} - 4 \times 10^{17}$ molecules/cm^3 have been measured to within an error bound of $\pm$ 12 percent. The precision of the current calibration is limited primarily by the signal to noise ratio of the observed $O_2(a)$ EPR absorption spectra. Recommendations for improving the precision of the diagnostic are presented. Since the performance of COIL devices is primarily controlled by the yield of singlet oxygen, $[O_2(a)]/[O_2(X)]$, the development of a diagnostic for $O_2(X)$, or yield directly, should be a priority for COIL research.

REFERENCES

1. Avizonis, P., et al., "Report to the American Physics Society of the Study Group on Science and Technology of Directed Energy Weapons", :Rev Mod Phys, 59(3), Part II, July 1987.

2. Watanabe, K., Kashiwabara, S., and Fujimoto, R., "Efficiency of Chemical Oxygen-Iodine Lasers: Theoretical Simulation and Experiment", J Appl Phys, 59(1), 42, 1 January 1982.

3. Heidner, R.F. III, Gardner, C.E., Segal, G.I., and El-Sayed, T.M., "Chain Reaction Mechanism for I_2 Dissociation in the $O_2(^1\Delta)$-I Atom Laser", J Phys Chem, 87(13), 2348, 1983.

4. Benard D.J., and Pchelkin, N.R., "Measurements of $O_2(^1\Delta)$ Content in the Gaseous Effluent of a Chemical Generator", Rev Sci Instrum, 49, 794, 1978.

5. Goldberg, I.B. and Laeger, H.O., "Electron Paramagnetic Resonance Transition Probabilities of Gas Phase Molecular Oxygen", J Phys Chem, 84, 3040, 1980.

6. Falick, A.M., Mahan, B.H., and Myers, R.J., "Paramagnetic Resonance Spectrum of the $^1\Delta_g$ Oxygen Molecule", J Chem Phys, 42(5), 1837, 1 March 1965.

7. Miller, T.A., "Rotational Moment, Rotational g Factor, Electronic Orbital g Factor, and Anisotropy of the Magnetic Susceptibility of $^1\Delta$ O_2", J Chem Phys, 54(1), 330, 1 January 1971.

8. Thomas, D.M., "A Parametric Study of the Production of $O_2(^1\Delta)$ by Microwave Excitation", USAF Academy Dept of Physics, Colorado Springs, Colorado, 30 June 1976.

9. Falick, A.M., "An EPR Study of the $O_2(^1\Delta_g)$ Molecule", Ph.D. Thesis, University of California at Berkley, June 1967.

REFERENCES (Continued)

10. Conn, P.K., "Engineering Development of a Singlet Delta Oxygen Generator", AFWL-TR-80-144, Weapons Laboratory, Kirtland AFB, New Mexico, May 1981.

11. Hurlock, S., Schwamb, D., and Davis, J., Oxygen-Iodine Supersonic Technology Program , AFWL-TR-84-37, Vol 1, Part 3, March 1985.

12. Berg, J.O., Oxygen-Iodine Supersonic Technology, AFWL-TR-85-43, Vol 1, Part 1, Weapons Laboratory, Kirtland AFB, New Mexico, October 1985.

13. Steinfeld, J.I., Molecules and Radiation, MIT Press, Massachusetts Institute of Technology, Cambridge, Massachusetts, 1974.

14. "Atomic Transition Probabilities: Hydrogen Through Neon", NSRDS-NBS 4, Vol I. Wiesse, W.L., Smith, M.W., Glennon, B.M. 5-20-60.

15. Lowe, J.P., Quantum Chemistry, Academic Press, New York, New York, 1978.

16. Wasserman, H.H., and Murray, R.W., Singlet Oxygen, Academic Press, New York, New York, 1979.

17. Bagder, R.M., Wright, A.C., and Whitlock, R.F., "Absolute Intensities of the Discrete and Continuous Absorption Bands of Oxygen Gas at 1.26 and 1.065 μm and the Radiative Lifetime of the Singlet-Delta State of Oxygen", J Chem Phys, 43, 4345, 1965.

18. Babcock, H.D., and Herzberg, L., "Fine Structure of the Red System of Atmospheric Oxygen Bands", Astrophysical J, 108, 167, 1948.

19. Herzberg, L, and Herzberg, G., "Fine Structure of the Infrared Atmospheric Oxygen Bands", Astrophysical J, 105, 353, 1947.

20. Noxon, J.F., "Observation of the $(b^1\Sigma_g^+-a^1\Delta g)$ Transition in O_2", Can J Phys, 39, 1110, 1961.

REFERENCES (Cont.)

21. Nichols, R.W., "Franck-Condon Factors to High Vibrational Quantum Numbers V: O2 Band Systems", <u>Journal of Research of the National Bureau of Standards: A. Physics and Chemistry</u>, <u>69A</u>, No 4, 369, Aug 1965.

22. Herzberg, G., <u>Molecular Spectra and Molecular Structure: I. Spectra of Diatomic Molecules</u>, Van Nostrand Reinhold Co, New York, New York, 1950.

23. Goldberg, I.B., "Electron Spin Resonance Spectroscopy", <u>Treatise on Analytical Chemistry</u>, 2nd Ed, P.J. Elving, Editor, Part 1, Vol 10, J. Wiley and Sons, New York, New York, 1983.

24. Carrington, A., Levy, D.H., and Miller, T.A., "Electron Resonance of Gaseous Diatomic Molecules", <u>Advances in Chemical Physics</u>, Vol XVIII, Editors I. Prignonin and S.A. Rice, J Wiley and Sons, New York, NY 1970.

25. Tinkham, M., and Strandberg, M.W.P., "Theory of the Fine Structure of the Molecular Oxygen Ground State", <u>Physical Review</u>, <u>97</u>(4), 937, 15 February 1955.

26. Westenberg, A.A., and de Hass, N., "Quantitative Measurements of Gas Phase O and N Concentrations by ESR", <u>J Chem Phys</u>, <u>40</u>(10), 3087, 15 May 1964.

27. Davies, J.T., and Vaughan, J.M., "A New Tabulation of the Voight Profile", <u>Astrophysical Journal</u>, <u>137</u>, 1302.

28. Wilson, G.V.H., "Modulation Broadening of NMR and ESR Line Shapes", <u>J Appl Phys</u>, <u>34</u>(11), 3276, Nov 1963.

29. Reeves, G.K., and Wilson, G.H.V., "The Analysis of Modulation-Broadened Mode Admixed Lorentz Magnetic Resonance Line Shapes", <u>J Phys D: Appl Phys</u>, 1970, Vol 3, 1609, 1970.

30. Arndt, R., "Analytical Line Shapes for Lorentzian Signals Broadened by Modulation", <u>J Appl Phys</u>, <u>36</u>(8), 2522, Aug 1965.

REFERENCES (Cont.)

31. Tykarski, L., "The Modulation Broadening in Broad Lorentzian EPR Lines",
     J Phys D: Appl Phys, 7, 786, 1974.

32. Smith, G.W., "Modulation Effects in Magnetic Resonance: Widths and
     Amplitudes for Lorentzian and Gaussian Lines", J Appl Phys, 35(4), 1217,
     April 1964.

33. Perram, G.P. and Hager, G.D., The Standard Chemical Oxygen-Iodine Laser
     Kinetics Package, AFWL-TR-88-50, Weapons Laboratory, Kirtland AFB, New
     Mexico, Oct 1988.

34. Knickelbein, M.B., Marsh, K.L., Ulrich, O.T., and Bush, G.E., "Energy
     Transfer Kinetics of Singlet Molecular Oxygen: The Deactivation Channel
     for $O_2(b^1\Sigma_g^+)$", J Chem Phys, 87(4), 2392, 15 August 87.

35. Heidner, R.F III. "Behavior of Singlet Oxygen in the Oxygen-Iodine
     Transfer Laser", Photochem, 25, 449, 1984.

36. Wyatt, C.L., Radiometric Calibration: Theory and Methods, Academic Press,
     New York, New York, 1978.

37. Heidner, R.F. III, Gardner, C.E., El-Sayed, T.M., Segal, G.I., and
     Kasper, J.V.V., "Temperature Dependence of $O_2(^1\Delta)+O_2(^1\Delta)$ and
     $I(^2P_{1/2})+O_2(^1\Delta)$ Energy Pooling", J Chem Phys, 74(10), 5618, 15 May 1981.

38. Lilenfeld, H.V., Bradburn, G.R., and Hovis, F.E., Oxygen-Iodine Laser
     Kinetics, AFWL-TR-84-151, Weapons Laboratory, Kirtland AFB, New Mexico,
     October 1985.

39. Van Benthem, M.H., and Davis, S.J., "Detection of Vibrationally Excited
     I_2 the Iodine Dissociation Region of Chemical Oxygen-Iodine Lasers", J
     Phys Chem, 90, 902, 1986.

40. E-LINE CENTURY SERIES EPR spectrometer system, Model E-112 EPR System,
     Publication Number 87-125-044 Varian Instrument Division, Palo Alto,
     California.

REFERENCES (Concluded)

41. Kays, W.M., and Crawford, M.E., Convective Heat and Mass Transfer, McGraw-Hill, New York, New York, 1986.

42. Crowell, P.G., Deactivation of $O_2(^1\Delta)$ and $O_2(^1\Sigma)$ in a Channel of Arbitrary Cross Sectional Area, Report 82A/K-14-0.1682, R&D Associates, Albuquerque, NM, 12 April 1982.

43. Westenberg, A.A. and de Hass, N., "Observation on ESR Linewidths and Concentration Measurements of Gas Phase Radicals", J Chem Phys 51(12), 5215, 15 Dec 1969.

44. Crannage, R.P., Johnson, D.E., Dorko, E.A., Surface Quenching of Singlet Delta Oxygen, PL-TR-91-1013, Weapons Laboratory, Kirtland AFB, New Mexico, July 1991.

45. Bevington, P.R., Data Reduction and Error Analysis for the Physical Sciences, McGraw-Hill, New York, New York, 1969.

List Of Symbols

Symbol	Description
[Y]	concentration of chemical specie Y
M	arbitrary collision partner
l_i	orbital angular momentum for electron i
s_i	spin of electron i
$\underline{S}$	total electronic spin (atomic)
$\underline{L}$	total orbital angular momentum (atomic)
$\underline{J}$	total angular momentum (atomic)
Σ	total electronic spin (molecular)
Λ	total orbital angular momentum (molecular)
$\underline{K}$	rotational angular momentum
v'	excited electronic state vibrational quantum #
v"	ground electronic state vibrational quantum #
T_e	electronic energy
ω_e	harmonic vibrational constant
$\omega_e x_e$	anharmonic vibrational constant
$\omega_e y_e$	2nd anharmonic vibrational constant
B_e	rotational constant
α_e	2nd rotational constant
μ	magnetic dipole moment
H	magnetic field
M_s	quantum number for projection of spin onto magnetic field axis
M_J	quantum number for projection of total angular momentum onto magnetic field axis

List of Symbols (Continued)

Symbol	Description
H_o	incident field strength
T_m	period of magnetic field modulation
μ_z	projection of magnetic dipole onto field axis
μ_B	Bohr Magneton
g	Lande' g-factor (spectroscopic splitting factor)
g_L	spectroscopic splitting factor for orbital angular momentum
g_J	spectroscopic splitting factor for total angular momentum
g_{eff}	effective spectroscopic splitting factor = $(h/\mu_B)\, d\nu/dH$
E	energy
E_{rot}	rotational energy
ΔE	energy difference between two states
h	Planck's constant
ν	frequency of radiation
α	absorption
Γ	Lorentzian line shape's half width at half maximum
B_o	rotational spectroscopic constant for $v = 0$
k_i	kinetic rate coefficient for reaction i
P	total pressure
T	gas temperature
k_B	Boltzmann's constant
ξ	$[O_2(a^1\Delta)]/[O_2(^3\Sigma)]$
f	line shape function
α'	derivative of absorption, $d\alpha/dH$

List of Symbols (Continued)

Symbol	Description
$[N_i]$	concentration of specie N in state i
$[N_T]$	total concentration of specie N
Z	molecular partition function
$|\mu_{ij}|$	transition probability for magnetically induced transition
G_i	ESR gain setting for state i
I_i	integrated ESR area for state i
H_M	ESR magetic field modulation amplitude
P_μ	ESR incident microwave power
S_i	ESR intensity factor for state i
Φ_e	radiant flux
L_e	radiance
L_p	photon sterisent
Ω	solid angle
A	area
θ	angle
A_{ij}	spontaneous emission rate for state i to j
V	viewing volume
r	radial distance
λ	wavelength
c	speed of light
f	lens focal length
C_p	heat capacity
R	detector responsivity
D^*	detector detectivity

List of Symbols (Concluded)

Symbol	Description
NEP	detector noise equivalent power
Q	cavity quality
v	velocity
a	speed of sound
M	mach number
dP/dx	pressure gradient in the flow direction
$\dot{n}$	molar flow rate
l	length
a_o	aperature radius
μ	gas viscosity
r_o	tube radius
$\dot{m}$	mass flow rate
m	mass
ρ	density
x	distance in flow direction
τ	transmission
CAL_i	calibration factor for detector i
$\hat{r}$	correlation coefficient
σ	standard deviation
ΔH_{pp}	peak-to-peak magnetic line width
$\Delta \nu_G$	Gaussian line width
$\Delta \nu_L$	Lorentzian line width
η	Voight profile parameter